

Universidade de São Paulo  
Instituto de Astronomia, Geofísica e Ciências Atmosféricas  
Departamento de Geofísica

Felipe Baiadori da Silva

**Joint numerical modelling of  
thermomechanical and surface processes in  
the post-rift evolution of the Recôncavo,  
Tucano and Jatobá basins**

São Paulo

2024



Felipe Baiadori da Silva

**Joint numerical modelling of  
thermomechanical and surface processes in  
the post-rift evolution of the Recôncavo,  
Tucano and Jatobá basins**

Dissertação apresentada ao Departamento de Geofísica do Instituto de Astronomia, Geofísica e Ciências Atmosféricas da Universidade de São Paulo como requisito parcial para a obtenção do título de Mestre em Ciências.

Área de Concentração: Geofísica

Orientador: Prof. Dr. Victor Sacek

São Paulo

2024



# Acknowledgements

Agradeço ao Prof. Dr. Victor Sacek pela valiosa orientação, paciência, e amizade desde os meus anos de graduação e durante todo o desenvolvimento deste trabalho.

À minha família, pelo amor e apoio, indispensáveis em cada passo desta jornada.

À Fundação Coordenação de Aperfeiçoamento de Pessoal de Nível Superior (CAPES), pelo apoio financeiro, sob o projeto nº: 88887.638901/2021-00;

Aos professores e colegas do Departamento de Geofísica, pelo acolhimento e conhecimentos compartilhados;



# Resumo

Silva, F. B. (2024). *Modelagem conjunta de processos termomecânicos e superficiais na evolução pós-rifte das bacias do Recôncavo, Tucano e Jatobá*. Dissertação de Mestrado, Instituto de Astronomia, Geofísica e Ciências Atmosféricas, Universidade de São Paulo, São Paulo.

Processos erosivos e deposicionais atuando na superfície da Terra são responsáveis pela redistribuição de material, alterando a configuração de cargas aplicadas sobre a litosfera ao longo do tempo. A resposta isostática ao deslocamento destas cargas é principalmente determinada pelas propriedades reológicas da crosta e manto superior, e exerce influência direta na evolução da paisagem. Muitos estudos foram realizados com êxito ao longo das últimas décadas a fim de entender a extensão desta influência majoritariamente em contextos tectonicamente ativos. Como resultado, poucos trabalhos tiveram como foco o ajuste isostático relacionado à denudação durante períodos de quiescência tectônica. Neste trabalho, eu investigo a evolução da paisagem no sistema de rifte Recôncavo-Tucano-Jatobá (NE Brasil) durante a fase pós-rifte usando um modelo numérico termomecânico, auxiliado por variados vínculos geológicos e geofísicos, para simular a resposta dinâmica da litosfera à denudação diferencial ocorrida na região após o estiramento. Constata-se que o padrão de soerguimento observado afetando os flancos de vales fluviais na área é adequadamente explicado por mecanismos flexurais, contanto que o grau de acoplamento litosférico seja baixo. Ainda, a curvatura dos estratos Aptianos mapeados na região aponta uma baixa ( $\lesssim 5$  km) espessura elástica efetiva para o sistema de bacias, em conformidade com algumas estimativas anteriores na literatura. Propõe-se que o estado pouco acoplado da litosfera que melhor ajusta as observações pode ser devido a uma combinação de fatores térmicos e

litológicos, envolvendo o efeito térmico da cobertura sedimentar, a perturbação do campo de temperaturas relacionada a um *underplating* magmático, e alteração das rochas crustais inferiores pela interação com fluidos magmáticos em ascensão.

Palavras-chave: modelagem numérica, evolução da paisagem, bacia de Tucano, isostasia flexural.



# Abstract

Silva, F. B. (2024). *Joint modelling of thermomechanical and surface processes in the post-rift evolution of the Recôncavo, Tucano and Jatobá basins*. Dissertação de Mestrado, Instituto de Astronomia, Geofísica e Ciências Atmosféricas, Universidade de São Paulo, São Paulo.

Erosive and depositional processes acting on the surface of the Earth are responsible for the redistribution of material, changing the configuration of loads applied on the lithosphere over time. The isostatic response to the shifting of these loads is mainly determined by the rheological properties of the crust and upper mantle, and exerts a direct influence on the evolution of the landscape. Many studies have been successfully performed over the last decades in order to understand the extent of this influence mostly in tectonically active settings. As a result, few works have placed focus on the isostatic adjustment related to denudation during periods of tectonic quiescence. In this work I investigate the evolution of the landscape in the Recôncavo-Tucano-Jatobá rift system (NE Brazil) during the post-rift stage using a thermomechanical numerical model, aided by various geological and geophysical constraints, to simulate the dynamic response of the lithosphere to the differential denudation which took place in the region after rifting. It is found that the uplift pattern observed to affect the flanks of river valleys in the area is adequately explained by flexural mechanisms, provided that the degree of lithospheric coupling is low. Moreover, the curvature of the Aptian strata mapped in the region points at a low ( $\lesssim 5$  km) effective elastic thickness for the basin system, in accordance with some previous estimates in the literature. It is proposed that the weakly-coupled state of the lithosphere found to fit the observations may be due to a combination of the thermal and lithological factors, involving

the thermal effect of the sedimentary cover, perturbation of the temperature field related to magmatic underplating, and alteration of lower crustal rocks by interaction with rising magmatic fluids.

Keywords: numerical modelling, landscape evolution, Tucano basin, flexural isostasy.

# List of Figures

1.1	Schematic illustration of the joint influence of thermomechanical and surface processes on the lithosphere, in this case in a rift-related setting (modified from Bishop (2007)). . . . .	18
2.1	(a) Geological map of the Recôncavo-Tucano-Jatobá intracontinental rift, emphasizing the distribution of the Aptian sedimentary units composing the Marizal Formation; (b) topographic map of the region, using data from the ETOPO 2022 digital elevation model with a spatial resolution of 15 arc-seconds (MacFerrin et al., 2022); (c) geological profile A-A' showing the landscape and geometry of the sedimentary strata belonging to the São Sebastião and Marizal Formations (profile location is shown in panel b). Panels a and c are adapted from Freitas et al. (2017). SFR: São Francisco River; VBR: Vaza-Barris River; IR: Itapicuru River; BC: Baixa do Chico; SBG: Santa Brígida Graben; UP: Umburana Platform; CF: Caritá Fault; PLSZ: Pernambuco Lineament Shear Zone. Approximate location of the PLSZ from Oliveira et al. (2023). . . . .	23
2.2	Chronostratigraphic chart for the Central and South Tucano grabens, placing the Marizal Formation as post-rift deposits (adapted from Costa et al. 2007b). . . . .	28
2.3	Depiction of a few of the models proposed for the evolution of the RTJ rift: (a) crustal detachment model from Ussami et al. (1986); (b) double rifting model suggested by Castro (1987); (c) flexural cantilever model proposed in Magnavita et al. (1994). Modified from Döring et al. (2022). . . . .	32

3.1	Numerical setup adopted for the simulations. The thicknesses of the air, upper and lower crustal layers are, respectively: $h_{\text{air}} = 40$ km, $h_{\text{upper}} = h_{\text{sed}} + h_{\text{base}} = 20$ km, and $h_{\text{lower}} = 20$ km, where $h_{\text{sed}} = h_{\text{base}} = 10$ km are the respective thicknesses of the sediment fill and upper crustal basement. The total thickness of the lithosphere is $h_{\text{litho}} = 100$ km. The upper panel shows the initial topographic curve between 687 km and 1000 km. Blue curves show the yield strength envelope for the cases where $C = 1$ (solid curve) and $C = 10$ (dashed curve), assuming $\dot{\epsilon}_{II} = 10^{-14}$ s <sup>-1</sup> , $c_0 = 20$ MPa, and $\phi = 15^\circ$ ; red curve corresponds to the initial thermal configuration as a function of depth; and orange horizontal lines in the upper panel indicate the lateral extent of the compensation zones (see text) projected onto the profile. . . . .	46
4.1	Evolution of the second invariant of the strain rate tensor for the reference scenarios with $C$ of 10 (left column) and 1 (right column) for the lower crust, during a simulation period of 40 Myr. . . . .	52
4.2	Patterns of strain accumulated over a simulation period of 40 Myr for the reference scenarios, as well as topographic curves and stratal geometries resulting from the respective simulations. Horizontal extent shown is limited to the region of the constraining profile (687 to 1000 km). . . . .	53
4.3	Evolution of the second invariant of the strain rate tensor for two scenarios with (left column) and without (right column) compensation zones. Both simulations feature $C = 1$ for the lower crust. . . . .	55
4.4	Modelled uplift for scenarios with lower crustal $C$ of 10 (upper panel) and 1 (lower panel), with (blue curves) and without (red curves) off-profile denudation. Orange horizontal lines mark the location and extent of compensation zones. BCCZ = Baixa do Chico Compensation Zone, VBCZ = Vaza-Barris Compensation Zone, ICZ = Itapicuru Compensation Zone. . . . .	56

4.5	(a) Initial model topography and envelope (black dashed curve); (b-c) topographic and envelope curves resulting from the reference simulations; (d) final curves for a scenario accounting for off-profile denudation with $C = 1$ for the lower crust; (e) Geologic profile and erosive envelope from Freitas et al. (2017), reduced of the regional component. The observed erosive envelope (blue dashed curve) is plotted in panels b-d for comparison. . . .	57
4.6	Cosine similarity as a function of the lower crustal viscosity scaling factor $C$ .	58
4.7	Uplift curve along the profile from Freitas et al. (2017) (upper panel), and absolute value of the local curvature of the uplift (lower panel). Curvature values are calculated as the absolute value of the second derivative of the uplift approximated by means of a second-order finite difference approximation. The curve in the lower panel was smoothed using a Savitzky-Golay filter with a window size of 101 points and polynomial degree of 5. Red patches indicate the approximate wavelength of the uplift “pulses” associated with the Vaza-Barris and Itapicuru incisions. . . . .	61
4.8	Maximum curvature of a plate subject to periodic loading as a function of load wavelength for different $T_e$ values (3, 5, 12, and 25 km). Black dashed line indicates Earth’s mean curvature, and the wavelength interval compatible with the uplift over the Vaza-Barris and Itapicuru valleys is indicated by the yellow patch. . . . .	62
4.9	Distribution of the thermal perturbation ( $T - T_0$ ) with depth calculated using Equation 4.6 for $t = 0, 1, 0, 5, 1$ and 5 Myr. Horizontal dashed line indicates the top of the lower crust (thickness of 20 km) assuming the underplating occurs immediately beneath its base. . . . .	63
4.10	(a) Steady-state temperature profiles with (orange) and without (blue) sedimentary thermal blanketing, calculated by a simple numerical code using the finite difference approximation to the one-dimensional heat conduction equation, assuming adiabatic temperature increase in the asthenosphere; (b) temperature difference $\Delta T$ between the profiles in (a). . . . .	64



# List of Tables

3.1	Physical and rheological parameters for each layer in the simulations. Values extracted from Karato and Wu (1993) for olivine and from Gleason and Tullis (1995) for quartz. DO=dry olivine; WO=wet olivine; numerical values for referred constants are: $A_{\text{air}} = 1,0 \times 10^{-18}$ , $A_{\text{quartz}} = 8,574 \times 10^{-28}$ , $A_{\text{DO}} = 2,4168 \times 10^{-15}$ , $A_{\text{WO}} = 1,393 \times 10^{-14}$ , $H_{\text{uc}} = 9,26 \times 10^{-10}$ , and $H_{\text{lc}} = 2,86 \times 10^{-10}$ . . . . .	39
-----	---	----





# Contents

1. <i>Introduction</i> . . . . .	17
1.1 Processes acting on the lithosphere . . . . .	17
1.2 Objectives . . . . .	19
1.3 Dissertation outline . . . . .	20
2. <i>Geological Context</i> . . . . .	21
2.1 Tectonic and structural framework . . . . .	21
2.2 Sedimentary infill . . . . .	25
2.3 RTJ evolution models . . . . .	31
2.4 Post-rift evolution . . . . .	35
3. <i>Methods</i> . . . . .	37
3.1 Model equations . . . . .	37
3.2 Finite Element formulation . . . . .	40
3.3 Model setup . . . . .	45
3.4 Numerical procedures . . . . .	48
4. <i>Results</i> . . . . .	51
4.1 Reference models . . . . .	51
4.2 Off-profile denudation . . . . .	54
4.3 Degree of lithospheric coupling . . . . .	56
4.4 Discussion . . . . .	59
5. <i>Conclusions</i> . . . . .	67

*Bibliography* . . . . . 69

## Introduction

### *1.1 Processes acting on the lithosphere*

Tectonic forces affecting the lithosphere are responsible for actively reshaping the landscape, bringing about high-relief topography (Burov and Poliakov, 2001). Simultaneously, erosive mechanisms act upon the created relief, promoting the redistribution of rock and soil mass over the surface of the Earth (Figure 1.1). When the magnitude of erosive action shows significant spatial variation, it is termed differential denudation. The occurrence of differential denudation, both in periods of active tectonism as well as in the subsequent interval of relative quiescence, imposes stresses on the lithosphere, thus inducing further deformation as a consequence of flexural (mechanical) loading/unloading (Silva and Sacek, 2022). Moreover, the effect of a significant sedimentary cover having lower thermal conductivity with respect to the underlying basement rocks is to alter the geothermal gradients (Wangen, 1994), a fact bearing relevance when considered in the context of the subsidence history in sedimentary basins. In addition, the rheological properties of lithospheric and asthenospheric rocks play a fundamental role in the pattern of subsurface deformation and, as a consequence, in the evolution of topographic features.

Interest in the development of large-scale topographic attributes arises, among other reasons, from this very link between surface (erosive and depositional) and deeper thermo-mechanical processes. Through this connection, it is possible to make inferences regarding, for example, subsurface rheology and the thermal evolution of the lithosphere, as well as acquire knowledge of what physical parameters control the geological products related to these processes. This knowledge, in turn, finds application in various fields, particularly in constraining assessments of fluid reservoir potential and characterization, given that

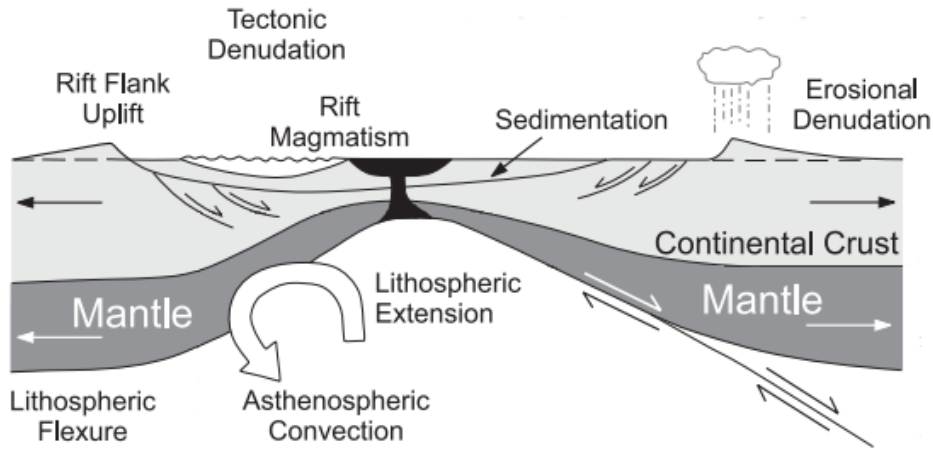


Figure 1.1: Schematic illustration of the joint influence of thermomechanical and surface processes on the lithosphere, in this case in a rift-related setting (modified from Bishop (2007)).

maturation depths are strongly temperature-dependent (Palumbo et al., 1999).

The joint influence exerted by the cited processes, as well as the complexity often inherent to their individual description and to feedback mechanisms between them, make it rather difficult to quantitatively trace, in a detailed manner, how the landscape progresses over time. Analytical solutions to problems of geodynamic concern, although valuable for the self-evident character of their derivations and ease of computational evaluation, are limited to formulations with largely simplified geometries and/or temporal evolution (e.g., the McKenzie (1978) pure shear model of rift evolution), and are usually able to explain only first-order features of the system under study (Brune, 2016; van Zelst et al., 2021).

In order to investigate more closely the products of the interplay between geodynamic and surface processes in the various tectonic contexts, a different approach must be considered. Numerical modelling is a powerful resource for understanding geophysical processes which fall beyond the reach of analytical methods, such as the effect of radiogenic heating of the crust, nonlinear rheologies and, importantly, complex geometries and boundary conditions (Brune, 2016). In spite of all that, the employment of numerical methods is not free from its own drawbacks. An example of such obstacles is presented when the modelled system necessarily involves large contrasts in physical properties between contiguous layers, a circumstance which often compromises the stability of the obtained solution (van

Zelst et al., 2021). In particular, problems involving time integration of a free surface tend to give rise to numerical instabilities related to this free surface, and several methods for preventing them have been proposed (Kaus et al., 2010; Cramer et al., 2012; Rose et al., 2017).

Many numerical models developed over the last few decades to investigate the evolution of rift-related regions (passive margins in particular) fall in one of two categories (Silva and Sacek, 2022): models with the goal of studying the evolution of the landscape, mostly emphasizing the post-rift stage and often representing isostatic compensation using thin-plate flexural theory (see Braun (2018) for a review); and others dedicated to delineating the main controls on rift evolution and architecture from a thermomechanical viewpoint (these are reviewed in Brune (2016)). Some of the more recent developments in numerical codes for geodynamical, lithosphere-scale problems were aimed at analysing the influence of the feedback between surface and deep-lithospheric thermomechanical processes on rift evolution (Theunissen and Huisman, 2019; Wolf et al., 2022). In spite of these developments, considerably fewer works have conducted numerical experiments with a coupled surface-thermomechanical model to closely inspect how the lithosphere responds mechanically to differential denudation during the tectonically quiescent period following extension and, specifically, the detailed progression of landforms associated with this response *after* intense tectonic action has ceased.

## 1.2 Objectives

Bearing in mind the previous introduction, this dissertation seeks a possible explanation for the significant short-wavelength uplift currently observed affecting the flanks of the Vaza-Barris and Itapicuru rivers which drain the Recôncavo-Tucano-Jatobá (RTJ) rift system in northeast Brazil, by means of a thermomechanical software coupled to a long-term landscape evolution model. In a more general sense, this provides an opportunity for learning more about how the feedback between erosion and Earth's interior dynamics determines the produced landscape as a function of lithospheric rheology and pattern of denudation.

### 1.3 *Dissertation outline*

The general structure of the present document is as follows: chapter 2 provides, in some detail, an account of the geological context involving the studied region, including its structural and tectonic setting, some aspects concerning the stratigraphy and depositional environments of the infill, a summary of the models proposed for the evolution of the region over the last few decades, and a description of the post-rift landscape evolution; chapter 3 is devoted to the thermomechanical model used in this work, i.e., the set of equations to be solved numerically when simulating mantle dynamics, their finite element formulation, the setup employed for the numerical scenarios, and the procedures operated by the code during a typical simulation; chapter 4 presents the results of the reference simulations and other most relevant scenarios, as well as an analysis of the adequacy of each scenario to the set of observations and a discussion of these results in terms of lithospheric flexure; finally, in chapter 5 concluding remarks are made which summarize the main points of the work.

## Geological Context

The RTJ intracontinental rift is located in the Brazilian northeastern margin, and is comprised of three linked sedimentary basins (namely: Recôncavo, Tucano and Jatobá basins). Its total areal extent is estimated to be 47.000 km<sup>2</sup>, with a contribution of 11.500 km<sup>2</sup> from the Recôncavo basin, 30.500 km<sup>2</sup> from the Tucano basin, and 5.000 km<sup>2</sup> from the Jatobá basin (Silva et al., 2007; Costa et al., 2007a,b). This region has been a target of intensive hydrocarbon exploration since the first oil reservoir discoveries during the 1940's (Milani and Davison, 1988), with greater detail of geophysical and geological data in the southern parts of the rift at first (Magnavita and Cupertino, 1988). In this chapter, the geological background for the RTJ rift will be presented, along with geophysical data relevant in constraining model setup and results.

### *2.1 Tectonic and structural framework*

The rift presents itself as a roughly N-S trending elongated feature in the East Atlantic margin of Brazil (Figure 2.1a), with a sharp change in rift trend direction to ENE-WSW near the western limits of the Jatobá basin. Its development is thought to be linked to that of the Camamu-Almada and Jacuípe offshore basins, usually interpreted as an aborted branch of the rift associated with the break-up of Gondwana and the opening of the South Atlantic ocean in the Early Cretaceous (Matos, 1992; Magnavita et al., 1994; Gordon et al., 2017).

In terms of structure, the framework observed in the RTJ rift is a relatively complex one. The rift traverses the boundary between the São Francisco and Borborema structural provinces (Gordon et al., 2017). Important differences must be noted between the

tectono-magmatic histories of these two provinces, particularly the cratonic character of the lithosphere comprising the São Francisco Province which, together with the other major South American cratonic areas (the Amazonian and Rio de la Plata cratons), formed the interiors of plates involved in the amalgamation of West Gondwana (Alkmim and Martins-Neto, 2012). As a result, the provinces exhibit distinct lithologies and structural patterns in the respective basements. The basement of the São Francisco Province is constituted by granitic-gneissic complexes, featuring intrusions of varying composition (ranging from granitic to mafic-ultramafic), and cut by structures trending N-S (Almeida et al., 1981), whereas the Borborema Province is characterized by fold systems associated with the Pan-African/Brasiliano orogenic event, and sectioned by a large system of E-W trending faults merging to the southwest with the Transbrasiliano shear zone (Almeida et al., 1981; Oliveira and Medeiros, 2018). Moreover, the Borborema Province represents the locus of intersection of two Brazilian margins with very different tectonic deformation patterns, namely the East Atlantic (characterized by basins mainly associated with extensional tectonics) and the Equatorial (featuring complex shear-dominated basins) margins, corresponding to different branches of the Atlantic rift system (Matos, 1992). Thus, the architecture of the RTJ, as well as the obliquity of the rift trend (N-S) relative to the direction of extension (roughly NW-SE), are strongly influenced by the differences in structural framework of the underlying basement blocks (Magnavita, 1992; Gordon et al., 2017).

Five asymmetrical half-grabens separated by basement highs and transverse features with general NW orientation comprise the RTJ basin system. Three of the half-grabens correspond to subdivisions of the Tucano basin (South, Central and North Tucano), and the Recôncavo graben can be further divided into eastern and western sub-basins separated by the Boa União and Dom João basement highs (Milani and Davison, 1988; Blaich et al., 2008).

The Recôncavo graben is bounded to the north and northwest by the Aporá High, to the south by the Barra fault system, to the west by the Maragogipe fault, and to the east by the Salvador fault system (Silva et al., 2007). This graben is characterized by a number of extensional faults trending NE (most frequently, N30°E), dipping NW in the western sub-basin and SE in the eastern sub-basin, and a smaller set of N40°W-trending faults interpreted as transfer faults accommodating extension rates varying between distinct compartments of the basin (Milani and Davison, 1988; Silva et al., 2007). The basement upon



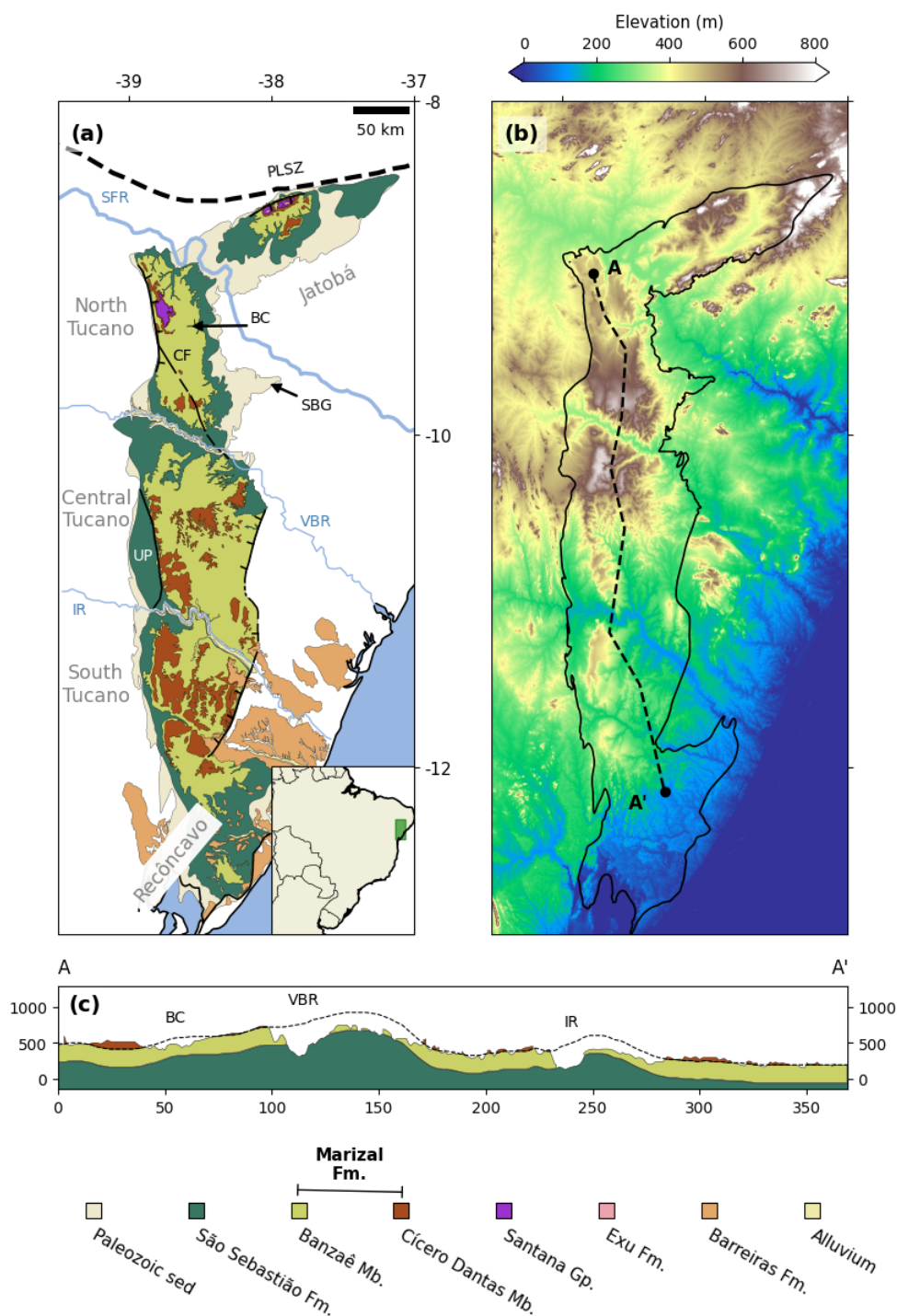


Figure 2.1: (a) Geological map of the Recôncavo-Tucano-Jatobá intracontinental rift, emphasizing the distribution of the Aptian sedimentary units composing the Marizal Formation; (b) topographic map of the region, using data from the ETOPO 2022 digital elevation model with a spatial resolution of 15 arc-seconds (MacFerrin et al., 2022); (c) geological profile A-A' showing the landscape and geometry of the sedimentary strata belonging to the São Sebastião and Marizal Formations (profile location is shown in panel b). Panels a and c are adapted from Freitas et al. (2017). SFR: São Francisco River; VBR: Vaza-Barris River; IR: Itapicuru River; BC: Baixa do Chico; SBG: Santa Brígida Graben; UP: Umburana Platform; CF: Caritá Fault; PLSZ: Pernambuco Lineament Shear Zone. Approximate location of the PLSZ from Oliveira et al. (2023).

which the Recôncavo basin was formed reaches a maximum depth exceeding 6.5 km at the Camaçari Low, and consists mainly of Archean granulitic gneisses, Neoproterozoic metasedimentary rocks, and minor occurrences of mafic rocks interpreted as remnants of ancient oceanic crust (Silva et al., 2007).

The South and Central Tucano grabens are separated by the Itapicuru transfer fault, responsible for offsetting the Inhambupe and Adustina border faults, thus constituting an interbasin transfer zone (Gawthorpe and Hurst, 1993; Costa et al., 2007b). It has been suggested that the tectonic styles for the two sub-basins are similar, with the basement and sedimentary layers dipping towards SE, and the main extensional fault system being comprised of domino-style faults with highest frequency of orientation at N25°E and synthetic with respect to the basins' border faults (Milani and Davison, 1988; Chemale et al., 1994; Costa et al., 2007b). In spite of exhibiting similar structural framework, estimated maximum basement depths differ greatly between the two sub-basins: 7 km in the South Tucano graben (Olindina and Inhambupe Lows), and over 16 km in the Central Tucano (Cícero Dantas Low) (Magnavita and Cupertino, 1988; Costa et al., 2007b; Alvarez and Holz, 2022), the anomalously large depths in the latter possibly originated from the merger between the Adustina border fault with the Duas Serras release fault (Alvarez and Holz, 2022).

Further north, the Central and North Tucano sub-basins are separated by the Vaza-Barris transfer zone, a structural feature trending NW-SE bounded to the north by the Caritá fault system (Milani and Davison, 1988; Freitas et al., 2017). Gravity data integrated to surface mapping of geological structures in this region sheds light on what is perhaps the most notable feature of the RTJ: the location of the depocenter (and master fault) shifts across the Vaza-Barris zone, with the border fault located to the east of the Central Tucano graben, and to the west of the North Tucano graben (Milani and Davison, 1988; Blaich et al., 2008; Gordon et al., 2017). This transfer zone, which is ~125 km long and over 30 km wide, has been referred to in the literature as Vaza-Barris Arch in association with its arcuate geometry at depth (Magnavita and Cupertino, 1988), and links the Adustina (Central Tucano) and São Saité (North Tucano) border faults, the former being apparently extended towards NW as the Caritá fault system (Gomes et al., 2018). The presence of a transfer zone connecting two basin border fault segments with opposite dip polarity is thought to exert important influence in basin stratigraphy and geomorphology

and, thus, the drainage pattern (Gawthorpe and Hurst, 1993), as evidenced by the close match between the Vaza-Barris river and its namesake accommodation zone. Additionally, Almeida Filho and Miranda (1997) suggested, based on application of digital image processing and enhancement techniques to gravity data from the RTJ, that the North Tucano sub-basin depocenter is composed of two structural lows (Salgado do Melão and Raso da Catarina Lows) separated by a basement high, to which the authors propose the name Raso da Catarina High.

The Jatobá graben exhibits a ENE-WSW orientation, differing largely from main trend directions throughout the remainder of the rift system. The structural pattern observed in this basin shows highest fault orientation frequency at N75°E, with fewer occurrences of faults trending NE-SW (Milani and Davison, 1988). Its master fault, named Ibimirim Fault, is located at the northern border of the basin, thus preserving the asymmetry established in the North Tucano graben. To the northeast, the Ibimirim Fault merges the Pernambuco Lineament, a 700 km-long shear zone located within the Borborema Province and trending ENE-WSW.

## 2.2 Sedimentary infill

The sedimentary strata comprising the stratigraphic record in the RTJ show ages between Paleozoic and Cenozoic (Figure 2.2). Sediments of Paleozoic age are grouped into the Paleozoic Supersequence, which may be divided in strata of Silurian/Devonian, Carboniferous, and Permian ages, preserved mostly in the North Tucano and Jatobá sub-basins and Santa Brígida graben, although restricted occurrences of Permian sediments have been identified in wells drilled in the South and Central Tucano sub-basins, and the Recôncavo basin (Milani and Davison, 1988; Magnavita and Cupertino, 1988; Caixeta et al., 1994; Costa et al., 2007a; Silva et al., 2007).

Silurian/Devonian sediments are represented by the Jatobá Group, which includes the Tacaratu and Inajá Formations, outcropping in the Santa Brígida graben located to the south of the Jatobá graben and to the east of North Tucano graben (Magnavita and Cupertino, 1988; Caixeta et al., 1994). The Tacaratu Formation is comprised mostly of coarse-grained sediments, being represented by polymictic conglomerates and conglomeratic arcose, whereas the Inajá Formation is characterized by cross-stratified fine- to

coarse-grained sandstones alternated with clay deposited by fluvial systems active during the Devonian (Caixeta et al., 1994; Costa et al., 2007a). These sediments are correlative to Paleozoic strata observed in the Parnaíba basin (Serra Grande and Canindé Groups) to the northwest (Caixeta et al., 1994; Caputo and Santos, 2020).

The Carboniferous deposits are ascribed to the Curitiba Formation, its reported occurrences being mostly from the Santa Brígida graben and the North Tucano sub-basin, and, to a lesser extent, the Jatobá basin. This formation is described as being composed of argillaceous sandstones, varved shales and limestones, which are interpreted as being deposited in a glacial environment (Costa et al., 2007a).

Strata of Permian age are more widespread throughout the rift system. In the North Tucano graben, Permian sedimentation is represented by the Santa Brígida Formation, which is divided into two members: Caldeirão, characterized by red siltous sediments and arcose, with evidence of eolian deposition; and Ingá, containing fine to coarse sandstones, calciferous siltstones, green shales and dark-coloured dolomites rich in organic matter, possibly deposited in a transitional to shallow marine environment (Caixeta et al., 1994; Costa et al., 2007a). To the south, the Permian Afligidos Formation constitutes the entire Paleozoic Erathem in the Central and South Tucano sub-basins, and Recôncavo basin. This stratigraphic unit is subdivided into the Pedrão and Cazumba Members, the former being composed of red shales, sandstones reworked by waves and evaporites; and the latter consisting of pelites and red lacustrine argillaceous sediments with occurrences of anidrite nodes, both members being deposited during the transition between a shallow marine and a lacustrine environment (Caixeta et al., 1994; Costa et al., 2007b; Silva et al., 2007).

The pre-rift sedimentary section of the RTJ begins with the deposition of the Brotas Group in the Late Jurassic, formed by the Aliança and Sergi Formations, which occur throughout the rift system with a maximum thickness of ~800 m in the Recôncavo basin, thinning progressively north and reaching a thickness of approximately 400 m in the North Tucano and Jatobá basins, although the Capianga Member thickens northwards (Silva et al., 2007; Costa et al., 2007a). Furthermore, the top of the pre-rift strata is represented by the Early Cretaceous Itaparica and Água Grande Formations, the latter seemingly absent in the Jatobá basin (Costa et al., 2007a). Pre-rift sediments consist of continental red beds related to fluvial-eolic cycles (Boipeba Member, Sergi and Água Grande Formations) alternating with lacustrine transgressions (Capianga Member and Itaparica Formation)

(Magnavita and Cupertino, 1988; Milani and Davison, 1988; Costa et al., 2007b).

Several authors (such as Caixeta et al. (1994), Silva et al. (2007), Costa et al. (2007a), Costa et al. (2007b), among others) consider the onset of the rifting stage to be marked by the deposition of the lacustrine pelites of the Tauá Member of the Candeias Formation on top of the fluvial-eolic Água Grande Formation, possibly associated to increased subsidence rates related to significant faulting of the crust, as well as an important change from an arid environment to a more humid climate (Caixeta et al., 1994; Silva et al., 2007). Though some works relate rifting initiation in the RTJ to the settling of the syn-tectonic Salvador Formation fanglomerates (Magnavita and Cupertino, 1988; Milani and Davison, 1988; Magnavita et al., 1994), Silva et al. (2007) argue that the deposition of these conglomerates could only take place after the implantation of the rift phase, since some time is required for rift flank uplift, erosion and subsequent alluvial fan formation to occur. Moreover, while Costa et al. (2007b) and other workers consider the rift stage sediments in the entire RTJ to be divided in two sequences (Early Berriasian to Early Hauterivian, and Early Hauterivian to Early Aptian), the seismic-stratigraphic analysis performed by Alvarez and Holz (2022) using data from the Tucano basin allowed the identification of seven unconformities in the Central Tucano graben, thus dividing the syn-rift infill of the graben in eight third-order sequences.

The Candeias Formation, deposited between Mid-Berriasian to Valanginian times, is divided into the Tauá and Gomo Members, the former being more evident in the Recôncavo graben and losing thickness towards the Central Tucano graben, where the Candeias Formation becomes undivided and continues to thin gradually throughout the remainder of the rift (Costa et al., 2007b). Sediments belonging to this formation are related to a lacustrine system (shales and turbiditic sandstones of the Gomo Member) installed when the structural framework of the rift was delineated, though not fully developed (Silva et al., 2007), and record an accentuated increase in subsidence rates associated to an augmentation of tectonic activity, thus reflecting a starved basin context with larger depths occurring in the Recôncavo graben (Costa et al., 2007b; Magnavita et al., 2012).

The decrease in subsidence rates which took place in the Valanginian, allied with increased sedimentation rates, allowed the previously starved Recôncavo basin to be significantly filled with sediments related to gravity flows, corresponding to the Maracangalha Formation, encompassing the Caruaçu layers and Pitanga Member (Silva et al., 2007). This

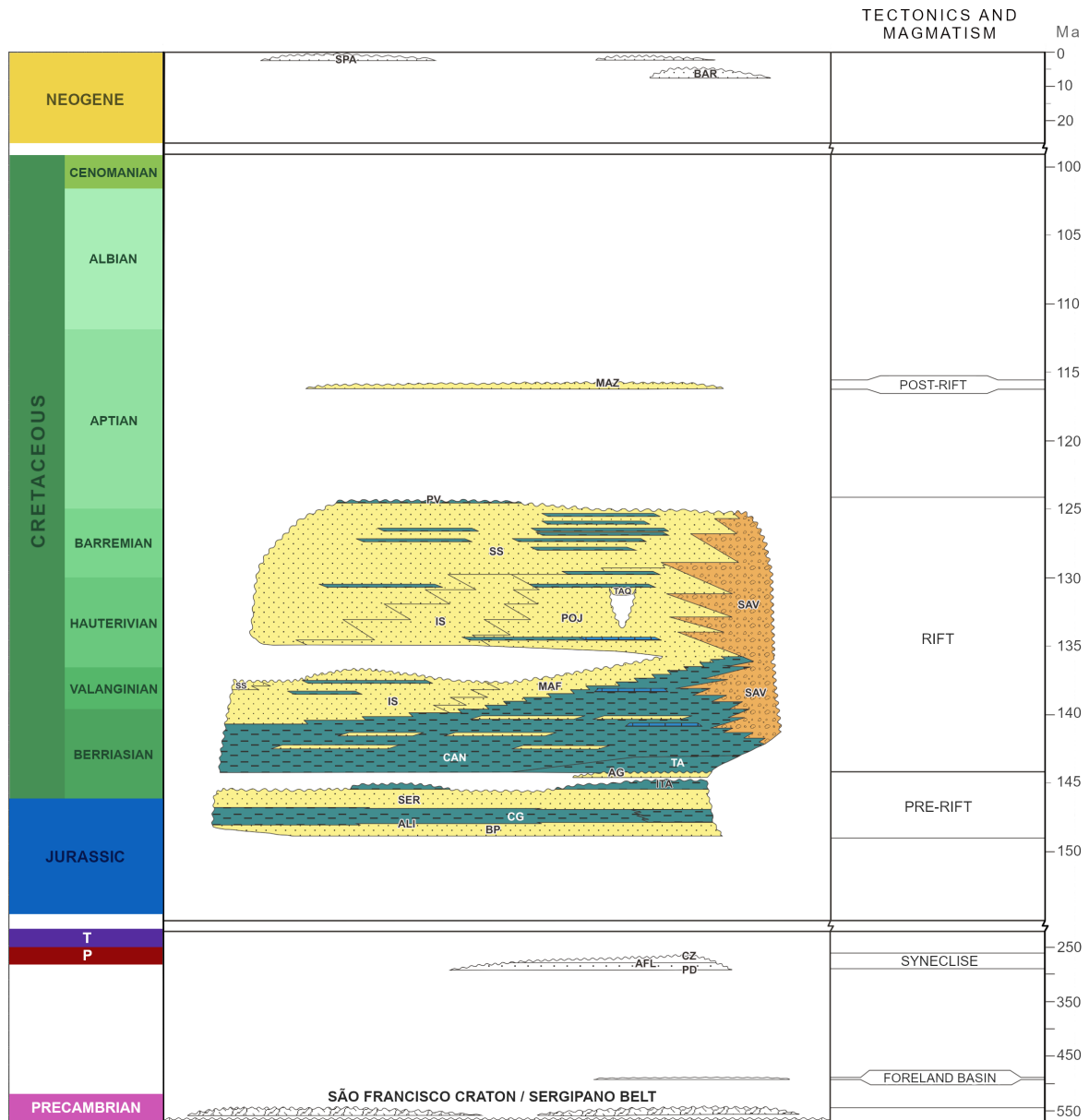


Figure 2.2: Chronostratigraphic chart for the Central and South Tucano grabens, placing the Marizal Formation as post-rift deposits (adapted from Costa et al. 2007b).

formation is characterized by gray shales and occurrences of sandstone lenses featuring cross-stratification and plane-parallel bedding, revealing the early stages of development of a deltaic system over a lacustrine setting (Caixeta et al., 1994; Silva et al., 2007). In the South and Central Tucano sub-basins, this fall in tectonic activity is manifested by the deposition of deltaic sediments composing the Ilhas Group, prograding from north to south (Costa et al., 2007b).

Later on, subdued tectonic activity made it possible for the deltaic system to expand to the southern portion of the rift, as indicated by the occurrence of Early Hauterivian deltaic sandstones belonging to the Marfim Formation in the Recôncavo basin, as well as deltaic-lacustrine cycles ascribed to the Pojuca Formation, which are related to an alternance between transgressive and regressive lacustrine systems in the rift (Silva et al., 2007; Costa et al., 2007b; Portela et al., 2016). Furthermore, during the Late Hauterivian the Taquipe Canyon was formed in a portion of the Recôncavo basin, representing a site for preferential lacustrine deposition (Taquipe Formation) amid the prevalence of deltaic sediments in the basin (Silva et al., 2007). The analysis of palynofacies encountered in the Pojuca strata in the Recôncavo graben, together with pyrolysis data from samples collected at outcrops, indicate that rocks belonging to this formation may constitute prolific hydrocarbon sources (Portela et al., 2016; Miranda et al., 2021).

During Late Hauterivian to Barremian, a new tectonic cycle was responsible for fault reactivation and accentuated subsidence rates, which were balanced by higher sedimentation rates in association to an inferred arid paleoclimate (Costa et al., 2007b). In this context, fluvial systems prevailed in the rift draining from north to south, as indicated by the fluvial sandstones of the São Sebastião Formation which lose thickness from the Jatobá graben towards the Recôncavo (Caixeta et al., 1994; Silva et al., 2007; Costa et al., 2007b). In some parts of the Tucano basin it is possible to observe the lacustrine shales and limestones of the Poço Verde Formation, with a thickness of about 110 m, topping the São Sebastião Formation, apparently indicating the end of the rifting stage (Costa et al., 2007b).

Alluvial sediments making up the Aptian-age Marizal Formation overlie the São Sebastião deposits, with an angular unconformity separating both sections (Magnavita and Cupertino, 1988; Costa et al., 2007b). The Marizal sediments are greatly exposed throughout the RTJ, particularly in the Tucano and Jatobá basins, and are commonly in-

terpreted as the sedimentary response to a post-rift thermal subsidence phase of the rift system (Magnavita and Cupertino, 1988; Milani and Davison, 1988; Costa et al., 2007a,b). Because the Aptian sedimentary units of the RTJ do not integrate the main hydrocarbon source system, the detailed sedimentologic and stratigraphic features of this succession have only recently begun to be studied. Figueiredo et al. (2016) investigated the causes for the observed decrease in sandstone and conglomerate maturity between the São Sebastião (quartz-rich) and Marizal (feldspar-rich) formations in the Tucano basin, by performing a provenance analysis on several conglomerates and conglomeratic sandstones as a means to determine temporal variations in proximal source areas. Their results point to a model including reactivation of border faults subsequent to erosional retreat of rift flanks.

Freitas et al. (2017) propose, based on detailed sedimentologic and stratigraphic descriptions of the Marizal Formation, a division of these deposits into the lower Banzaê and upper Cícero Dantas members, their contact being locally characterized by the fossiliferous Amargosa Bed associated with a marine transgression episode. The authors verified contrasting fluvial architectures between the two members composing the Marizal Formation and, supported by faults within these deposits observed by the same authors, propose that rifting activity may have extended through the deposition of the Banzaê Member. In addition, the analysis of deformation band structures in the Vaza-Barris transfer zone performed by Gomes et al. (2018) reveals that these subseismic-scale structures are well distributed throughout the transfer zone, reflecting the regional tectonic stress field at the time. Their presence was observed also in the Marizal Formation, corroborating the interpretation of Freitas et al. (2017) that the main rifting stage persisted through the Aptian (Gomes et al., 2018).

In certain areas of the North Tucano and Jatobá grabens, the Marizal sediments are observed to be coated by post-rift carbonate-bearing successions correlative to the Santana Group of the Araripe basin (Freitas et al., 2017). These successions are interpreted as the remaining portions of regional lacustrine carbonate deposits from the Aptian in association with a rise in base level, possibly relating several basins in the Brazilian northeast (Varejão et al., 2016). Furthermore, the carbonate successions are locally covered in the Jatobá basin by nonfossiliferous coarse to conglomeratic sandstones belonging to the Albian-aged Exu Formation, which is believed to have deposited in a fluvial braided to meandering environment (Neumann and Rocha, 2014).



## 2.3 RTJ evolution models

The lack of a thick sedimentary package unambiguously related to a post-rift sag phase in the RTJ has given rise over the last few decades to a number of different models to explain the rift's tectonic and stratigraphic evolution. Ussami et al. (1986) suggest, based on gravity and stratigraphic well data, that extension in the Tucano rift was limited to the upper crust, without significant deflection of the Moho immediately beneath the basin, as implied by the absence of positive Bouguer anomalies flanking the rift system. According to the authors, the lack of Moho upwarping is indicative of a large flexural rigidity (they estimate 50-80 km for the effective elastic thickness) for the lithosphere during and after the active phase of the rift. The model proposed in the same work supports the existence of a crustal detachment surface, as conceptualized by Wernicke (1985), linking the onshore Tucano and offshore Jacuípe basins. In this crustal detachment model, deep lithospheric thinning beneath the Jacuípe basin compensates for upper crustal thinning beneath the Tucano basin (Figure 2.3a). Castro (1987) points out that the model presented by Ussami et al. (1986) does not take into account the reversal in polarity of the rift, nor the crustal thinning in the São Francisco Craton as modelled in prior works, and proposes a double rifting model with multiple detachment surfaces for the evolution of RTJ system (Figure 2.3b).

Milani and Davison (1988) made use of 2D gravity modelling constrained by seismic data on four profiles in the RTJ. The modelled cross-sections were obtained by iteratively adjusting model geometries to fit a more detailed gravity dataset than that used by Ussami et al. (1986). Their results show an offset between calculated Bouguer anomaly minima and depocenter positions, as well as significant Moho relief coinciding with the areas of greatest subsidence in the rift, indicating that important amounts of thinning occurred at lower crustal levels as well. The authors invoke a slight rotation of the East Brazilian microplate, a triangular Precambrian block bordered to the west by the Tucano basin, as an important factor in the opening of the rift, emphasizing also the fundamental role of the preexisting structural framework in shaping this basin system. Their explanation for the absence of post-rift sediments is that, with a Moho relief such as the observed by the authors, both vertical and lateral heat conduction become important, thus cooling the lithosphere before the termination of the rift phase.

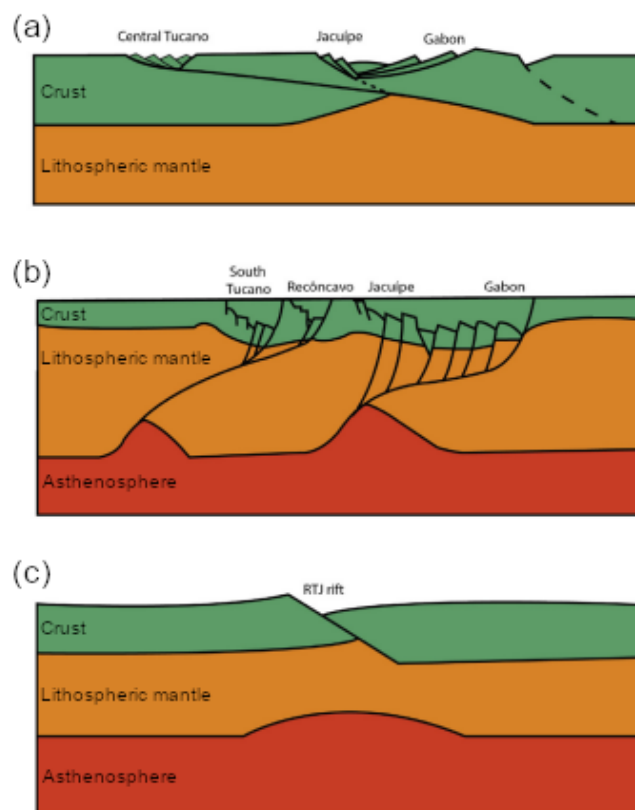


Figure 2.3: Depiction of a few of the models proposed for the evolution of the RTJ rift: (a) crustal detachment model from Ussami et al. (1986); (b) double rifting model suggested by Castro (1987); (c) flexural cantilever model proposed in Magnavita et al. (1994). Modified from Döring et al. (2022).

Karner et al. (1992) argue that porosity values estimated for the pre-rift successions in the Tucano basin do not support the existence, at any point, of an expressive post-rift sedimentary package in the basin, forwarding the interpretation of extension confined to the crust and balanced by means of intracrustal detachments. The referred work investigates the development of the Tucano rift by means of a kinematic analytical model which assumes the presence of a detachment surface with defined geometry horizontally offsetting the region extended by simple shear (upper crust) and that thinned by pure shear (lower crust and lithospheric mantle), subsequently calculating the isostatic readjustment associated with the change in lithospheric thermal configuration and including the effect of erosion. They find that first-order rift architecture and Bouguer gravity anomalies are best explained by the presence of an intracrustal detachment, or the retention of a relatively high flexural strength even after rifting, with an estimated post-rift effective elastic thickness of 30 km. Thus, the results presented in Karner et al. (1992) show some agreement with the interpretation of Ussami et al. (1986).

In contrast with preceding works, Magnavita et al. (1994) propose the occurrence of a regional erosional event to explain the lack of expressive thicknesses of post-rift sediments in the RTJ. The authors cite as evidence to this interpretation the shallow depths to the onset of maturity of organic matter implied by vitrinite reflectance data from the Recôncavo and South Tucano sub-basins, which point at over 1 km of eroded material (although the estimation of such a value is highly dependent on the assumed geothermal gradient). Moreover, they point out that the outcropping of early rift-phase sediments throughout these sub-basins is also indicative of widespread removal of sediments. A flexural cantilever model of continental extension (Figure 2.3c), as described in Kuszniir and Ziegler (1992), is applied in Magnavita et al. (1994) to simulate the rheological, thermal and flexural (regional) isostatic response of the RTJ lithosphere during rifting, whereby extension occurs as a combination of simple shear in the upper crust and pure shear in the lower crust and lithospheric mantle, and the flexural strength associated with the isostatic compensation is determined by the best-fit model of basin stratigraphy. Application of this model to the RTJ returns an effective elastic thickness value of 5 km for the modelled cross-sections. Furthermore, the aforementioned regional uplift is explained in the referred contribution by the presence of approximately 3.5 km of underplated magma possibly related to a more widespread magmatic event, as suggested by the observation of dolerite

dikes to the east of the Tucano basin (Magnavita et al., 1994).

The results of the analysis and quantitative modelling carried out by Mohriak et al. (2000) of an integrated onshore-offshore potential field dataset, constrained by deep seismic reflection profiles in the Tucano and Sergipe-Alagoas basins, reveal, according to the authors, the existence of two distinct zones of Moho upwarping: one, with lower amplitude, located slightly to the east of the Central Tucano sub-basin depocenter; and another located beneath the Sergipe-Alagoas basin. The model put forward by Mohriak et al. (2000) to explain these observations and the evolution of the Tucano/Sergipe-Alagoas system invokes widespread lithospheric extension during the initial stages of rifting, with basins beginning to form along preexisting crustal weak zones, subsequently shifting to a more localized extensional regime, thus defining the site of continental break-up to the east of the Sergipe-Alagoas basin. Also relying on crustal-scale gravity modelling, potential field and seismic reflection data analysis, Blaich et al. (2008) studied the onshore-offshore crustal structure correlation and morphology of the continent-ocean boundary in northeastern Brazil, observing strong along-margin variations in the distance between the continental hinge zone and the inferred location of the continent-ocean boundary, as well as changes in the asymmetric relationship between the conjugate Brazilian and West African margins. They interpret these changes as reflecting the dip of intracrustal detachments taking part in extensional basin formation, and propose that the evolution of the RTJ took place in a polyphase manner, that is, with pure shear and associated listric faulting characterizing the mode of extension during early rifting, and a later transition to a simple shear mode of upper crustal extension by means of detachment surfaces (Blaich et al., 2008).

More recently, Döring et al. (2022) evaluated the plausibility of many of the aforementioned extensional models for the RTJ from a seismological perspective, motivated by the ambiguity of previous gravity modelling attempts in the region. They investigated the crustal structure of the basin system through an analysis of teleseismic receiver functions from a number of seismic stations spread around the region of the Recôncavo, Tucano and Sergipe-Alagoas basins. The authors estimate that the crust beneath the Recôncavo and Tucano basins is  $\sim 41,6$  km thick, very similar to the thickness estimated for the adjacent São Francisco Craton (41,8 km), and significantly larger than that estimated for the Borborema Province (36,2 km). It is also found that a high-velocity, lower-crustal layer of considerable thickness (5-8 km) underlying the RTJ which is not observed beneath the

São Francisco and Borborema structural provinces. According to Döring et al. (2022), the most plausible interpretation is that this fast layer results from magmatic underplating, concluding that the results corroborate the flexural cantilever model forwarded by Magnavita et al. (1994).

Alvarez and Holz (2022) carried out seismic-stratigraphic interpretations, as well as spectral analysis and modelling using gravity data, focusing on the Central Tucano sub-basin. The modelled transects suggest greater crustal thinning beneath the Tucano basin compared to the Recôncavo and Jatobá basins, with the crust-mantle interface occurring at particularly shallow depths ( $\sim 24$  km) below the Cícero Dantas Low, where estimated sediment thicknesses reach over 16 km. The authors' interpretation is that the presence of such significant thinning of the crust in this region is indicative of the influence of heterogeneities in crustal rheology reflecting the contrasting structural frameworks of the São Francisco Craton and the Borborema Province, as supported by Milani and Davison (1988). In addition, the obtained gravity models feature a high-density layer ( $3000 \text{ kg.m}^{-3}$ ) underlying the lower crust which can be correlated to that found by Döring et al. (2022), indicative of possible magmatic underplating and, thus, supporting the interpretation of Magnavita et al. (1994).

## 2.4 Post-rift evolution

Despite the multitude of models proposed for the syn-rift evolution of the RTJ, far fewer were developed concerning its progress during the subsequent period of tectonic quiescence. Important aspects of the post-rift (i.e., Late Cretaceous onwards) stage of the RTJ system are recorded on its present landscape. First among them, and of great importance to this work, are the elevations bordering the main river valleys (Figure 2.1b,c). These features show a strongly three-dimensional morphology characterized by a short wavelength, comparable to the transversal dimensions of the basin system. Moreover, the elevated valley flanks are located in different sub-basins: the northernmost uplifted flank is placed in the Northern Tucano graben, while its southernmost counterpart occurs in the Central Tucano. They are roughly symmetrical in terms of elevation with respect to the Vaza-Barris incision, and coincide with areas where the Marizal Formation is well preserved (Figure 2.1c). In particular, the summit of the elevation to the north approximately

correlates with occurrences of the Cícero Dantas member.

Some deep-rooted, syn-tectonic structures, such as the Carité fault and the Umburana Platform eastern fault, hold spatial relations to the uplifted Vaza-Barris flanks. The Carité fault “traverses” the northern flank, but shows minor topographic expression. Close to the western border of the Central Tucano, the Umburana Platform fault appears to limit the occurrence of the Marizal sediments, though its influence on the magnitude of the adjacent uplift seems to be only secondary. From these observations one might infer that the elevation of river incision flanks in the RTJ is only weakly, if at all, controlled by the activity of syn-rift structures and, thus, may well have originated during the post-rift phase of the basin system. This inference is reinforced by the strong correlation between the borders of elevated terrains and the drainage pattern within the basin, hinting at a possible mechanism for the uplift based on the flexural isostatic response of the lithosphere to sediment removal along fluvial incisions.

Alternatively, Freitas et al. (2017) suggested that differential compaction may have been responsible for the observed deformation, based on the position of the synform of the Aptian strata roughly over rift depocenters. However, close inspection of the position and orientation of the antiforms and synforms axes show a remarkable shift from the asymmetrical distribution of depocenters along the Tucano basin. Moreover, the uniformity of the thickness of the Banzaê layer throughout most of the RTJ and the close match between stratal antiforms and main river flanks favor the hypothesis that the deformation of Aptian units might be primarily due to flexural uplift.

## Methods

As the present work was developed through the use of the thermomechanical numerical code Mandyoc (acronym for MAntle DYnamics simulatOR Code), described in Sacek et al. (2022) and applied to a diversity of lithosphere-related geodynamical problems (e.g. Silva and Sacek, 2022; Salazar-Mora and Sacek, 2023; Silva et al., 2023), this chapter aims at detailing its physical and mathematical formulation, as well as the numerical implementation.

### 3.1 Model equations

Throughout geological time, the mechanical behaviour of Earth's mantle and crust resembles that of a non-Newtonian fluid, that is, described by a nonlinear relationship between stress and strain rate. In order to realistically reproduce mantle convection, Mandyoc solves the equations for conservation of mass, momentum, and energy (Zhong et al., 2007; Sacek et al., 2022):

$$u_{i,i} = 0 \quad (3.1)$$

$$\sigma_{ij,j} + \rho g \delta_{i2} = 0 \quad (3.2)$$

$$\frac{\partial T}{\partial t} + u_i T_{,i} = (\kappa T_{,i})_{,i} + \frac{H}{c_p} - \frac{u_2 g \alpha T}{c_p} \quad (3.3)$$

where

$$\sigma_{ij} = -P \delta_{ij} + \eta(u_{i,j} + u_{j,i}), \quad (3.4)$$

$$\rho(T) = \rho_0(1 - \alpha T), \quad (3.5)$$

$u_i$  represents the  $i$ -th component of the velocity vector,  $g$  is the gravity acceleration,  $T$  is the temperature,  $t$  is a time variable,  $\kappa$  is the thermal diffusivity,  $H$  is the radiogenic

heat production per unit mass,  $\rho$  is the effective density for mantle rocks (dependent on temperature and composition),  $\rho_0$  is the reference density at zero temperature,  $\alpha$  is the volumetric thermal expansivity,  $c_p$  is the specific heat capacity at constant pressure,  $P$  is the total pressure,  $\eta$  is the effective rock viscosity, and  $\delta_{ij}$  is the Kronecker delta, defined such that

$$\delta_{ij} = \begin{cases} 1, & i = j \\ 0, & i \neq j \end{cases}.$$

In the notation used to write equations 3.1-3.3, a comma is used to indicate differentiation with respect to that variable, and repeated indices are indicative of summation over the index. Thus, we could equivalently write  $u_{i,i} = 0$  in two dimensions as

$$\frac{\partial u_1}{\partial x_1} + \frac{\partial u_2}{\partial x_2} = 0.$$

The first term in the right-hand side of Eq. 3.3 corresponds to heat transported by conduction, the second term is associated to heat produced by radioactive decay in the rocks, and the third term represents adiabatic heating.

It is worth mentioning that certain assumptions underlie the form in which equations 3.1-3.3 were written. Firstly, the Boussinesq approximation for incompressible fluids was used in writing the equation for conservation of mass (Eq. 3.1). Secondly, the inertial term in the equation for conservation of momentum (Eq. 3.2), corresponding to the net acceleration of a given rock element, was taken to be negligible. The first approximation is applicable in the present circumstances because variations in rock density within the upper mantle are relatively small (van Zelst et al., 2021), whereas the second approximation is valid because, for highly viscous fluids, the magnitude of the inertial term is generally far smaller than that of gravitational and viscous resistance forces, as evidenced by the slow rate of change in plate velocities (Gerya, 2010).

The visco-plastic rheology adopted for the model features a nonlinear dependence of ductile viscosity on temperature and strain rate, given by:

$$\eta_{visc} = C \cdot A^{-\frac{1}{n}} \cdot \dot{\epsilon}_{II}^{\frac{(1-n)}{n}} \cdot \exp\left(\frac{Q + VP}{nRT}\right) \quad (3.6)$$

where  $A$  is a pre-exponential factor,  $n$  is the exponent of the power law,  $\dot{\epsilon}_{II}$  is the second invariant of the strain rate tensor,  $Q$  and  $V$  are, respectively, the activation energy and volume for viscous creep,  $P$  and  $T$  are the pressure and temperature,  $R$  is the universal



	Air	Sediment	Upper crust	Lower crust	Litho. mantle	Asthen.
Reference density (kg.m <sup>-3</sup> )	1	2500	2700	2800	3354	3378
Creep flow law	-	Quartz	Quartz	Quartz	DO	WO
$A$ (Pa <sup>-<math>n</math></sup> /s)	$A_{\text{air}}$	$A_{\text{quartz}}$	$A_{\text{quartz}}$	$A_{\text{quartz}}$	$A_{\text{DO}}$	$A_{\text{WO}}$
$Q$ (kJ/mol)	0	222	222	222	540	429
$n$	1	4	4	4	3,5	3
$V$ (m <sup>3</sup> /mol)	0	0	0	0	$25 \times 10^{-6}$	$15 \times 10^{-6}$
$H$ (W/kg)	0	$H_{\text{uc}}$	$H_{\text{uc}}$	$H_{\text{lc}}$	$9 \times 10^{-12}$	0

Table 3.1 - Physical and rheological parameters for each layer in the simulations. Values extracted from Karato and Wu (1993) for olivine and from Gleason and Tullis (1995) for quartz. DO=dry olivine; WO=wet olivine; numerical values for referred constants are:  $A_{\text{air}} = 1,0 \times 10^{-18}$ ,  $A_{\text{quartz}} = 8,574 \times 10^{-28}$ ,  $A_{\text{DO}} = 2,4168 \times 10^{-15}$ ,  $A_{\text{WO}} = 1,393 \times 10^{-14}$ ,  $H_{\text{uc}} = 9,26 \times 10^{-10}$ , and  $H_{\text{lc}} = 2,86 \times 10^{-10}$ .

gas constant, and  $C$  is a compositional factor introduced in Sacek (2017) to control the viscosity and simulate the rheological distinction between depleted and enriched mantle. This compositional factor also provides a way to easily vary the degree of coupling of the lithosphere (smaller values of  $C$  for the lower crust imply a “more weakly” coupled lithosphere). The values of the parameters  $A$ ,  $n$ ,  $Q$  and  $V$  for olivine and quartz are extracted from Karato and Wu (1993) and Gleason and Tullis (1995), respectively, and are shown in Table 3.1.

Faulting is simulated in the thermomechanical code by means of the Drucker-Prager criterion for (pressure-dependent) plastic deformation:

$$\sigma_{\text{yield}} = c_0 \cdot \cos\phi + P \cdot \sin\phi \quad (3.7)$$

where  $\phi$  is the angle of internal friction and  $c_0$  is a coefficient which reflects the internal cohesion of the rock. The effective viscosity is thus determined from both the viscous and the plastic components as:

$$\eta = \min(\eta_{\text{plast}}, \eta_{\text{visc}}) = \min\left(\frac{\sigma_{\text{yield}}}{2\dot{\epsilon}_{II}}, \eta_{\text{visc}}\right). \quad (3.8)$$

As chemical variations, both vertical and lateral, play an important role in mantle dynamics, Mandyoc evaluates the compositional scaling factor  $C$  at different points of the model domain during the simulation by means of the equation:

$$\frac{\partial C}{\partial t} + u_i C_{,i} = 0. \quad (3.9)$$

Equation 3.9 is solved using a number of tracer particles randomly positioned within each grid element (the number of particles per element is usually of the order of a few tens). Estimation of  $C$  at a particular node is done by interpolating over tracer particles surrounding that node (Tackley and King, 2003).

### 3.2 *Finite Element formulation*

In order to jointly solve equations 3.1-3.3 and investigate geodynamic processes acting in the interior of the Earth, it is necessary to make use of numerical methods. This is partly due to the nonlinearity introduced by the advective term in the energy conservation equation (Eq. 3.3). The problem at hand is further complicated when complex geometries and distribution of material properties within the Earth are to be simulated realistically (as occurs, for instance, when phase transitions in the mantle must be accounted for). For these reasons, the Finite Elements (FE) method was chosen to numerically solve the system of equations describing mantle flow.

Put simply, the FE method consists of formulating a given boundary value problem as a matrix equation (when possible) in order to estimate approximate values of the sought function (or functions) on a set of nodes approximating the problem domain. This is often achieved through application of the weighted residuals method to the given equations, resulting in the weak formulation of the problem. Approximations of the problem functions, as well as the weighting functions involved, are then constructed as linear combinations of given sets of so called shape functions, which, upon further manipulation, will result in the desired matrix formulation (Hughes, 2012). It is common for the shape functions adopted in FE solutions to be nonzero only near one node in the mesh, which results in the construction of a sparse matrix, allowing for greater computational efficiency in the implementation of the solution.

It must be noted that the finite element formulation for the first two equations (3.1 and 3.2) can be stated independently from that for the third equation, and that temporal variations need only be taken into account in the equation of conservation of energy, since the only time derivative appearing in the system is that of temperature in Eq. 3.3. Thus, the numerical solution of the coupled equations reproducing mantle convection is divided into steps, namely the finite element solution for the Stokes' flow to obtain the pressure

and velocity fields, and a separate formulation for the conservation of energy to obtain the temperature field (Zhong et al., 2007).

The statement of the weak formulation for the Stokes' flow problem, as described by equations 3.1 and 3.2, takes on the form:

$$\int_{\Omega} w_{i,j} \sigma_{ij} d\Omega - \int_{\Omega} q u_{i,i} d\Omega = \int_{\Omega} w_i f_i d\Omega + \sum_{i=1}^{n_{sd}} \int_{\Gamma_{h_i}} w_i h_i d\Gamma \quad (3.10)$$

where  $w_i$  and  $q$  are weighting functions,  $f_i = \rho g \delta_{i3}$ ,  $\Omega$  is the problem domain, and the boundary conditions are specified as

$$u_i = g_i \text{ on } \Gamma_{g_i}, \quad (3.11)$$

$$\sigma_{ij} n_j = h_i \text{ on } \Gamma_{h_i} \quad (3.12)$$

where  $\Gamma_{g_i}$  and  $\Gamma_{h_i}$  are the boundaries of  $\Omega$  associated with the first (essential) and second (natural) boundary conditions (note that the boundaries need not be the same for different values of  $i$ ),  $n_j$  represents the  $j$ -th component of the unit vector locally normal to boundary  $\Gamma_{h_i}$ , and  $g_i$  and  $h_i$  are prescribed functions. Equation 3.4 provides a way to rewrite  $\sigma_{ij}$  in terms of  $P$  and  $u_i$  in Equation 3.10:

$$\begin{aligned} & \int_{\Omega} w_{i,j} (-P \delta_{ij} + c_{ijkl} u_{k,l}) d\Omega - \int_{\Omega} q u_{i,i} d\Omega = \int_{\Omega} w_i f_i d\Omega + \sum_{i=1}^{n_{sd}} \int_{\Gamma_{h_i}} w_i h_i d\Gamma \\ \Rightarrow & \int_{\Omega} w_{i,j} c_{ijkl} u_{k,l} d\Omega - \int_{\Omega} q u_{i,i} d\Omega - \int_{\Omega} P u_{i,i} d\Omega = \int_{\Omega} w_i f_i d\Omega + \sum_{i=1}^{n_{sd}} \int_{\Gamma_{h_i}} w_i h_i d\Gamma \end{aligned} \quad (3.13)$$

where  $c_{ijkl}$  represents the elements of a fourth-rank tensor related to the material properties of the medium evaluated at the given point (in this case, the viscosity) by

$$c_{ijkl} = \eta (\delta_{ik} \delta_{jl} + \delta_{il} \delta_{jk})$$

The Galerkin weak formulation is achieved by further assuming that the velocity components may be written as  $u_i = v_i + g_i$ , where  $v_i = 0$  on  $\Gamma_{g_i}$  and  $g_i$  corresponds to the function appearing on the right-hand side of the essential boundary condition (Eq. 3.11). Hence:

$$\begin{aligned} & \int_{\Omega} w_{i,j} c_{ijkl} v_{k,l} d\Omega - \int_{\Omega} q v_{i,i} d\Omega - \int_{\Omega} w_{i,i} P d\Omega = \\ & = \int_{\Omega} w_i f_i d\Omega + \sum_{i=1}^{n_{sd}} \int_{\Gamma_{h_i}} w_i h_i d\Gamma - \int_{\Omega} w_{i,j} c_{ijkl} g_{k,l} d\Omega \end{aligned} \quad (3.14)$$

It is most convenient to rewrite the integrand in the first term of the left-hand side of Equation 3.14 as

$$w_{i,j}c_{ijkl}v_{k,l} = \boldsymbol{\varepsilon}(\mathbf{w})^T D \boldsymbol{\varepsilon}(\mathbf{v})$$

where, for two dimensional plane viscous flow,

$$\boldsymbol{\varepsilon}(\mathbf{v}) = \left\{ \begin{array}{c} v_{1,1} \\ v_{2,2} \\ v_{1,2} + v_{2,1} \end{array} \right\}, \quad D = \begin{bmatrix} 2\eta & 0 & 0 \\ 0 & 2\eta & 0 \\ 0 & 0 & \eta \end{bmatrix}.$$

As mentioned before, the velocity, pressure, and weighting functions are approximated by linear combinations of sets of shape functions:

$$\mathbf{v} = v_i \mathbf{e}_i = \sum_{A \in \Omega^v - \Gamma_{g_i}^v} N_A v_{iA} \mathbf{e}_i \quad (3.15)$$

$$\mathbf{w} = w_i \mathbf{e}_i = \sum_{A \in \Omega^v - \Gamma_{g_i}^v} N_A w_{iA} \mathbf{e}_i \quad (3.16)$$

$$\mathbf{g} = g_i \mathbf{e}_i = \sum_{A \in \Gamma_{g_i}^v} N_A g_{iA} \mathbf{e}_i \quad (3.17)$$

$$P = \sum_{B \in \Omega^P} M_B P_B \quad (3.18)$$

$$q = \sum_{B \in \Omega^P} M_B q_B \quad (3.19)$$

where  $\mathbf{e}_i$  is the  $i$ -th basis vector,  $\Omega^v$  and  $\Omega^P$  are the sets of nodes where one wishes to determine velocity and pressure, respectively;  $\Gamma_{g_i}^v \subset \Omega^v$  is the set of nodes approximating the boundary  $\Gamma_{g_i}$ ,  $N_A$  and  $M_B$  are the shape functions for velocity at node  $A$  and pressure at node  $B$ , respectively. The coefficients of the shape functions in each of the linear combinations are the values of the approximated function at the referred node. It may be noted that

$$\begin{aligned} \boldsymbol{\varepsilon}(\mathbf{w})^T D \boldsymbol{\varepsilon}(\mathbf{v}) &= \boldsymbol{\varepsilon} \left( \sum_{A \in \Omega^v - \Gamma_{g_i}^v} N_A w_{iA} \mathbf{e}_i \right)^T D \boldsymbol{\varepsilon} \left( \sum_{B \in \Omega^v - \Gamma_{g_j}^v} N_B v_{jB} \mathbf{e}_j \right) = \\ &= \sum_{A \in \Omega^v - \Gamma_{g_i}^v} w_{iA} \left[ \sum_{B \in \Omega^v - \Gamma_{g_j}^v} \boldsymbol{\varepsilon}(N_A \mathbf{e}_i)^T D \boldsymbol{\varepsilon}(N_B \mathbf{e}_j) v_{jB} \right] = \\ &= \sum_{A \in \Omega^v - \Gamma_{g_i}^v} w_{iA} \left[ \sum_{B \in \Omega^v - \Gamma_{g_j}^v} \mathbf{e}_i^T B_A^T D B_B \mathbf{e}_j v_{jB} \right] \end{aligned}$$

where, in two-dimensions,

$$B_A = \begin{bmatrix} N_{A,1} & 0 \\ 0 & N_{A,2} \\ N_{A,2} & N_{A,1} \end{bmatrix}.$$

Substitution of 3.15-3.19 into Equation 3.14 leads to

$$\begin{aligned} \sum_{A \in \Omega^v - \Gamma_{g_i}^v} w_{iA} \left[ \sum_{B \in \Omega^v - \Gamma_{g_i}^v} (\mathbf{e}_i^T \int_{\Omega} B_A^T D B_B d\Omega \mathbf{e}_j) v_{jB} - \sum_{B \in \Omega^P} \left( \int_{\Omega} M_B N_{A,i} d\Omega \right) P_B \right] - \\ - \sum_{A \in \Omega^P} \left[ q_A \sum_{B \in \Omega^v - \Gamma_{g_j}^v} \left( \int_{\Omega} M_A N_{B,j} d\Omega \right) v_{jB} \right] = \quad (3.20) \\ \sum_{A \in \Omega^v - \Gamma_{g_i}^v} w_{iA} \left[ \left( \int_{\Omega} N_A f_i d\Omega + \sum_{i=1}^{n_{sd}} \int_{\Gamma_{h_i}} N_A h_i d\Gamma \right) - \sum_{B \in \Gamma_{g_j}^v} (\mathbf{e}_i^T \int_{\Omega} B_A^T D B_B d\Omega \mathbf{e}_j) g_{jB} \right]. \end{aligned}$$

As 3.20 must hold regardless of the  $w_{iA}$  and  $q_A$ , we are left with the following equations:

$$\begin{aligned} \sum_{B \in \Omega^v - \Gamma_{g_i}^v} (\mathbf{e}_i^T \int_{\Omega} B_A^T D B_B d\Omega \mathbf{e}_j) v_{jB} - \sum_{B \in \Omega^P} \left( \int_{\Omega} M_B N_{A,i} d\Omega \right) P_B = \\ = \int_{\Omega} N_A f_i d\Omega + \sum_{i=1}^{n_{sd}} \int_{\Gamma_{h_i}} N_A h_i d\Gamma - \sum_{B \in \Gamma_{g_j}^v} (\mathbf{e}_i^T \int_{\Omega} B_A^T D B_B d\Omega \mathbf{e}_j) g_{jB}, \quad (3.21) \end{aligned}$$

$$\sum_{B \in \Omega^v - \Gamma_{g_j}^v} \left( \int_{\Omega} M_A N_{B,j} d\Omega \right) v_{jB} = 0 \quad (3.22)$$

which may be rewritten as a matrix equation:

$$\begin{bmatrix} K & G \\ G^T & 0 \end{bmatrix} \begin{Bmatrix} V \\ P \end{Bmatrix} = \begin{Bmatrix} F \\ 0 \end{Bmatrix} \quad (3.23)$$

where  $V$  is a vector storing the velocity components at all nodal points,  $P$  stores the pressure values at calculated pressure nodes,  $F$  represents the force vector composed of all terms on the right-hand side of Eq. 3.21,  $K$ ,  $G$  and  $G^T$  stand for the stiffness matrix, discrete gradient operator and discrete divergence operator, respectively (Zhong et al., 2007). The stiffness matrix elements are given by

$$K_{lm} = \mathbf{e}_i^T \int_{\Omega} B_A^T D B_B d\Omega \mathbf{e}_j \quad (3.24)$$

where  $1 \leq l, m \leq n_v n_{sd}$  are the global equation numbers corresponding to global node numbers  $A$ ,  $B$  and degrees of freedom  $i$ ,  $j$ , and  $n_v$  is the number of nodes in the velocity

mesh. The global equation numbers depend on the ordering of the solution vector components (whether the degree of freedom varies first and the node number varies second, or the inverse). The element formulation is achieved by dividing the solution domain  $\Omega$  into a number of elements with a given number of velocity and pressure nodes per element. One possible arrangement is to use elements containing four velocity nodes at the corners, and one pressure element at the center, yielding bilinear shape functions for the velocity, and a constant shape function for the pressure at each element. Zhong et al. (2007) stress the importance of maintaining the interpolation functions for velocity one order higher than those for pressure so as to avoid spurious solutions for the Stokes flow.

The FE formulation for Eq. 3.3 follows that presented in Braun (2003):

$$\mathbf{M}\dot{\mathbf{a}}_T + (\mathbf{K}_a + \mathbf{K}_c)\mathbf{a}_T = \mathbf{F} \quad (3.25)$$

where

$$\mathbf{M} = \int_{\Omega} \mathbf{N}^T \rho_0 c_p \mathbf{N} d\Omega \quad (3.26)$$

$$\mathbf{K}_a = \int_{\Omega} \mathbf{N}^T \rho_0 c_p \mathbf{v} \cdot \mathbf{B} d\Omega \quad (3.27)$$

$$\mathbf{K}_c = \int_{\Omega} \mathbf{B}^T k \mathbf{B} d\Omega \quad (3.28)$$

$$\mathbf{F} = \int_{\Omega} \mathbf{N}^T (H - \alpha g u_2 T) d\Omega. \quad (3.29)$$

In equations 3.25-3.29,  $\mathbf{a}_T$  and  $\dot{\mathbf{a}}_T$  are the solution vectors storing the temperature and its time derivative, respectively, at each mesh node;  $\mathbf{N}$  is a row vector of shape functions,  $\mathbf{B} \equiv \nabla \mathbf{N}$ , and  $\mathbf{v}$  is the velocity vector at the point of evaluation.

It may be observed in 3.25 that, while  $\mathbf{K}_c$  is a symmetric matrix,  $\mathbf{K}_a$  is not. This lack of symmetry associated with the advective term makes it so that the obtained solutions are devoid of the “best approximation” property, and become affected by spurious oscillations (“wiggles”) when high values of the Peclet number are involved (Brooks and Hughes, 1982; Zhong et al., 2007). To avoid the deterioration of solutions by numerical instabilities related to convection-dominated flows, a streamline upwind Petrov-Galerkin formulation (Brooks and Hughes, 1982) is implemented such that Equation 3.25 is slightly altered:

$$\mathbf{M}\dot{\mathbf{a}}_T + (\mathbf{K}_a^* + \mathbf{K}_c)\mathbf{a}_T = \mathbf{M}\dot{\mathbf{a}}_T + \mathbf{K}_T\mathbf{a}_T = \mathbf{F} \quad (3.30)$$

with

$$\begin{aligned}
\mathbf{K}_a^* &= \int_{\Omega} \mathbf{N}^{*\text{T}} \rho_0 c_p \mathbf{v} \cdot \mathbf{B} d\Omega \\
N_A^* &= N_A + \frac{\alpha_{\text{opt}} h^e \mathbf{v} \cdot \nabla N_A}{2|\mathbf{v}|} \\
\alpha_{\text{opt}} &= \coth(\text{Pe}) - \frac{1}{\text{Pe}} \\
\text{Pe} &= \frac{|\mathbf{v}| h^e}{2\kappa \rho_0 c_p},
\end{aligned} \tag{3.31}$$

$h^e$  being a characteristic element size in the direction of  $\mathbf{v}$ .

Temporal variations in the temperature field are resolved using the midpoint implicit scheme shown in Braun (2003), whereby the time derivative of the temperature is approximated by:

$$\frac{\mathbf{a}_T(t + \Delta t) - \mathbf{a}_T(t)}{\Delta t} = \theta \dot{\mathbf{a}}_T(t + \Delta t) + (1 - \theta) \dot{\mathbf{a}}_T(t) \tag{3.32}$$

where  $\theta$  is a parameter with a value set to 0.5. To obtain an expression for  $\mathbf{a}_T(t + \Delta t)$  in terms of  $\mathbf{a}_T(t)$ , one may multiply both sides of Equation 3.32 by  $\mathbf{M}(t + \Delta t)$  and make use of Equation 3.30, together with the assumption that  $\mathbf{M}(t + \Delta t)\mathbf{M}^{-1}(t) \approx \mathbf{I}$ . Thus, we have:

$$\begin{aligned}
\mathbf{M}(t + \Delta t) \left( \frac{\mathbf{a}_T(t + \Delta t) - \mathbf{a}_T(t)}{\Delta t} \right) &= \theta [\mathbf{F}(t + \Delta t) - \mathbf{K}_T(t + \Delta t) \mathbf{a}_T(t + \Delta t)] + \\
&+ (1 - \theta) [\mathbf{F}(t) - \mathbf{K}_T(t) \mathbf{a}_T(t)]
\end{aligned}$$

which, upon rearrangement, yields

$$\begin{aligned}
[\mathbf{M}(t + \Delta t) + \theta \Delta t \mathbf{K}_T] \mathbf{a}_T(t + \Delta t) &= [\mathbf{M}(t + \Delta t) - (1 - \theta) \Delta t \mathbf{K}_T(t)] \mathbf{a}_T(t) + \\
&+ \Delta t [\theta \mathbf{F}(t + \Delta t) + (1 - \theta) \mathbf{F}(t)].
\end{aligned} \tag{3.33}$$

### 3.3 Model setup

The adopted setup has horizontal and vertical dimensions of 1600 km and 300 km, respectively, divided in  $1 \times 1 \text{ km}^2$  finite elements. A free-surface stabilization algorithm based on the ‘‘sticky air’’ approach (Cramer et al., 2012) is implemented to adequately simulate the topography whereby a low-density layer with a viscosity smaller than that of the underlying rock layers (albeit much greater than the actual viscosity of air) is included. The thickness of the lithosphere is set to be 100 km, and includes three crustal

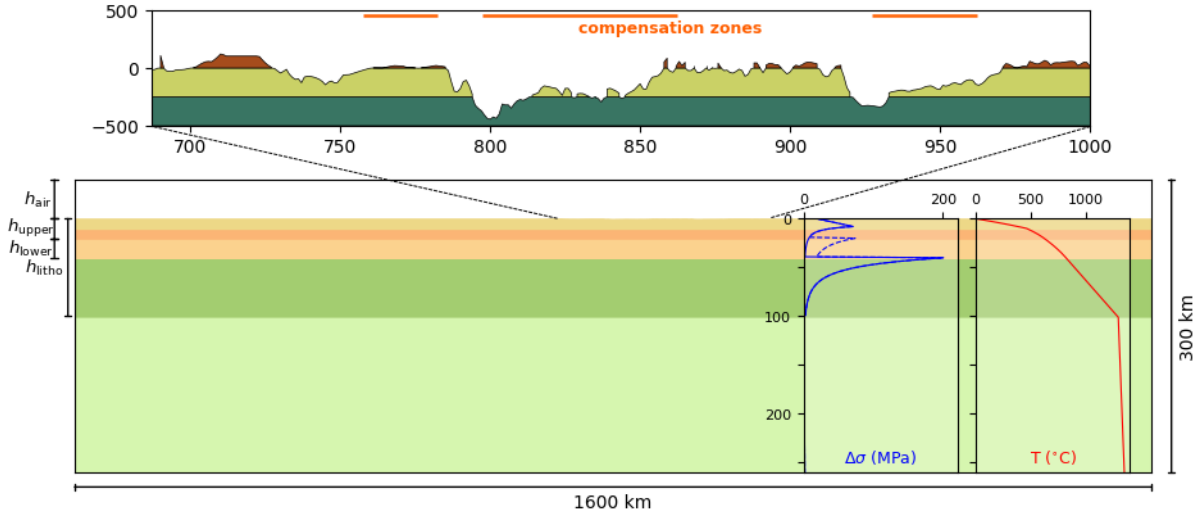


Figure 3.1: Numerical setup adopted for the simulations. The thicknesses of the air, upper and lower crustal layers are, respectively:  $h_{\text{air}} = 40$  km,  $h_{\text{upper}} = h_{\text{sed}} + h_{\text{base}} = 20$  km, and  $h_{\text{lower}} = 20$  km, where  $h_{\text{sed}} = h_{\text{base}} = 10$  km are the respective thicknesses of the sediment fill and upper crustal basement. The total thickness of the lithosphere is  $h_{\text{litho}} = 100$  km. The upper panel shows the initial topographic curve between 687 km and 1000 km. Blue curves show the yield strength envelope for the cases where  $C = 1$  (solid curve) and  $C = 10$  (dashed curve), assuming  $\dot{\epsilon}_{II} = 10^{-14} \text{ s}^{-1}$ ,  $c_0 = 20$  MPa, and  $\phi = 15^\circ$ ; red curve corresponds to the initial thermal configuration as a function of depth; and orange horizontal lines in the upper panel indicate the lateral extent of the compensation zones (see text) projected onto the profile.

layers (sediments, upper and lower crust) and the lithospheric mantle. The value used for crustal thickness is based on Döring et al. (2022). Interfaces between layers beneath the surface are all assumed to be initially horizontal. This assumption is made partly because, although variations in upper crustal thickness in the study region are recognized, these features were probably already isostatically compensated by the end of the rifting period and, thus, bear little relevance to the evolution of the basin system during the post-rift period. Moreover, a reasonably simplified geometry for the layers (as is the case) greatly contributes to the detailed understanding of the physical mechanisms responsible for the observed topography.

The initial thermal structure of the model lithosphere depends only on the vertical coordinate, and corresponds to the solution to the equation:

$$0 = \frac{\partial}{\partial z} \left( \kappa \frac{\partial T}{\partial z} \right) + \frac{H(z)}{c_p} \quad (3.34)$$

where  $H$  is the (depth-dependent) radiogenic heat production. This form of the heat equation accounts for vertical variations in the thermal conductivity (and, hence, diffusivity) of the rocks, thus allowing us to simulate the effect of thermal blanketing by sediments with



lower conductivity on the initial temperature field. To include the thermal influence of the sedimentary layer during subsequent time steps, the code was slightly modified such that the thermal diffusivity of elements where the density falls between 200 and 2600 kg.m<sup>-3</sup> is set to be lower than in the remaining mesh elements (the density assumed for the sediments is 2500 kg.m<sup>-3</sup>). The initial temperature profile in the asthenospheric mantle is described by the expression:

$$T(z) = T_p \cdot \exp\left(\frac{g\alpha z}{c_p}\right) \quad (3.35)$$

where  $T_p = 1262$  °C is the potential temperature assumed for the mantle. Boundary conditions for the temperature field are such that temperature values on the lateral boundaries of the model domain are free, while keeping the temperature on the top and bottom boundaries fixed.

A topographic-erosive profile from Freitas et al. (2017), subtracted of a regional topographic trend with wavelength longer than basin-scale, is used as a constraint for both shaping the initial surface of the hereby reported simulations, and the amount of sediment removed from each point of the profile. Although the numerical code features a variety of modes for the simulation of surface processes (Silva and Sacek, 2022), none of these give a detailed control over the eroded rock volume on each surface node. Thus, flexural loads due to denudation are modelled in the present work as the instantaneous removal of material from the surface of the model (interface between the air and sediment layers). This approach is justified by the fact that, since the thermal structure of the model does not vary significantly from the initial thermal setting (no perturbations of thermal or tectonic origin are assumed during the simulation), little change would be observed in the nonlinear mechanical behavior of the lithosphere if it was subjected to temporally distributed denudation in comparison with the adopted method.

The initial topographic form for each simulation is assumed to be the difference between the erosive envelope and the topographic curve in the profile reduced of the regional contribution. This initial curve is placed close to the center of the horizontal mesh, and the horizontal extent of the model domain (1600 km) is kept much greater than the total length of the profile ( $\sim 370$  km) so as to avoid the influence of boundary effects over simulation results.

A set of simulations was performed in which three zones of “artificial removal” (here referred to as compensation zones) were introduced within the sediment layer in order to

reproduce the effect of denudation in areas adjacent to the profile used as constraint (Figure 3.1). Two of these areas are identifiable in a geologic map as regions of great exposure of the São Sebastião Formation, such as observed west of the Vaza-Barris and Itapicuru river valleys. The third zone of compensation includes the effect of the denudation occurring to the east of the Baixa do Chico area, north of the Vaza-Barris, as a consequence of the presence of a significant fluvial incision which flows into the São Francisco River farther east.

In the compensation zones, three-dimensional removal of surface material is represented by a local decrease in sediment density. This density contrast between the zones and the surrounding sediment is calculated as follows: given the thickness  $h_{\text{off}}$  of off-profile denudated material and the depth of compensation  $d_{\text{comp}}$ , the decrease  $\Delta\rho$  in the density is

$$\Delta\rho g d_{\text{comp}} = \rho_{\text{sed}} g h_{\text{off}} \rightarrow \Delta\rho = \frac{\rho_{\text{sed}} h_{\text{off}}}{d_{\text{comp}}} \quad (3.36)$$

where  $\rho_{\text{sed}}$  is the density assumed for the sedimentary layer. Taking  $\rho_{\text{sed}} = 2500 \text{ kg.m}^{-3}$ ,  $h_{\text{off}} = 330 \text{ m}$ , and  $d_{\text{comp}} = 5 \text{ km}$ , one obtains  $\Delta\rho = 165 \text{ kg.m}^{-3}$ , yielding a value of  $\rho_{\text{comp}} = 2335 \text{ kg.m}^{-3}$  for the compensation zones.

### 3.4 Numerical procedures

Initial and boundary conditions for the velocity and temperature fields, along with the reference density  $\rho_0$ , radiogenic heat production  $H$ , and compositional scaling factor  $C$  for the viscosity in each layer are provided by the user at the beginning of each run. The effective viscosity is determined after calculation of  $\sigma_{\text{yield}}/2\dot{\epsilon}_{II}$  and  $\eta_{\text{visc}}$ , and the linear system arising from the finite element formulation of the equations for conservation of mass and momentum (3.1 and 3.2) is solved iteratively by means of the Uzawa scheme, as this method is less demanding in terms of computation compared to direct solution methods (Zhong et al., 2007). This yields a new configuration for the velocity and pressure fields in each mesh node, and the viscosity field is re-evaluated, which, in turn, implies further adjustments in the velocity field. Alterations of these fields in each time step of the simulation are performed until a certain convergence criterion is satisfied, given by:

$$\chi_f = 1 - \frac{\langle (f^i - \langle f^i \rangle) \cdot (f^{i+1} - \langle f^{i+1} \rangle) \rangle}{|f^i - \langle f^i \rangle| |f^{i+1} - \langle f^{i+1} \rangle|} \leq \text{tol} \quad (3.37)$$

---

where  $f$  is a vector storing the values of velocity components for each node of the mesh,  $tol$  is the tolerance parameter for the above criterion (here,  $tol = 1 \times 10^{-7}$ ) and  $\langle f^i \rangle$  stands for the mean value of  $f$ .

Mandyoc is written in C language, and distributed memory code parallelization is handled through the Portable, Extensible Toolkit for Scientific Computation (PETSc), which makes use of the MPI standard for all communication between different processes (Balay et al., 2019). Further information regarding Mandyoc, such as source code, contributing and licensing information may be freely consulted at <https://github.com/ggciag/mandyoc>.



## Results

In this chapter, results of the simulated thermomechanical scenarios bearing most relevance to this work are presented. In analysing each scenario, the subsurface distribution and evolution of such quantities as accumulated strain and strain rate throughout the simulation are essential, as is the resulting topographic form associated with a given thermomechanical setting. The chapter begins by introducing the results for the simulations arbitrarily chosen reference.

### *4.1 Reference models*

The scenarios set as comparative references to subsequent simulations feature the setup shown in Figure 3.1, and differ between each other only in the compositional scaling factor  $C$  for the lower crust:  $C = 10$  for the first reference scenario, and  $C = 1$  for the second. In both simulations, the remaining layers were assumed to have a compositional scaling factor of 1.

The first relevant aspect to be noted when jointly analysing the reference simulations is the manner in which the strain rate field evolves in each of these scenarios (Figure 4.1): both are characterized by initially high magnitudes of the strain rate spread over most of the model domain, due to the “sudden” removal of surface material in the beginning of simulation time, thus causing an abrupt perturbation in the subsurface stress field. Following the initial perturbation, the strain rate distribution differs significantly between the scenarios. In the scenario with  $C = 10$ , the strain rate distribution after 20 Myr is such that the highest magnitudes occur at depths greater than 100 km over large horizontal distances. In contrast, after the same 20 Myr period, the second reference scenario is

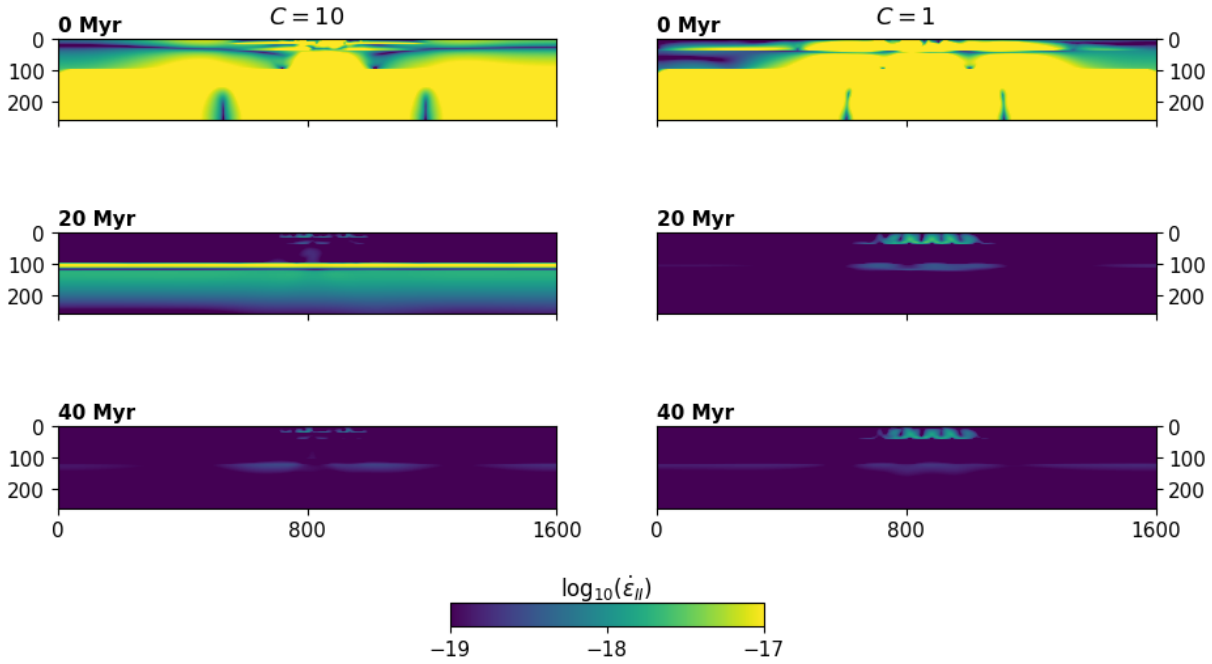


Figure 4.1: Evolution of the second invariant of the strain rate tensor for the reference scenarios with  $C$  of 10 (left column) and 1 (right column) for the lower crust, during a simulation period of 40 Myr.

marked by the concentration of high strain rates in lower crustal levels ( $\sim 40$  km depth), with significant strain rates affecting shallower layers in a much more laterally restricted region, the extent of which is extent roughly equal to that of the constraining profile.

In addition to differences in the strain rate pattern at a given instant, the evolution of these patterns between scenarios is also distinct: although high strain rates are observed at sublithospheric depths during the first  $\sim 20$  Myr in the scenario with  $C = 10$ , the values in subsequent time steps up to the end of the simulation are dramatically reduced throughout the model domain. Inspection of the strain rate field for the second reference scenario, on the other hand, shows that high magnitudes persist in the lower crust through the entire simulation with little change in intensity or lateral extent of the affected zone.

The temporal evolution of the strain rate in each of these scenarios hints at their respective accumulated strain patterns (Figure 4.2). As one might expect, for the first simulation, strain is mostly concentrated at the base of the lithosphere, with some strain occurring sporadically within the crust. The second reference model shows intense strain localization in the crust, with some deformation taking place in other parts of the model domain. Figure 4.2 also allows us to compare the resulting topographic curves and stratal geometries for each reference scenario. The topography resulting from the scenario with more viscous

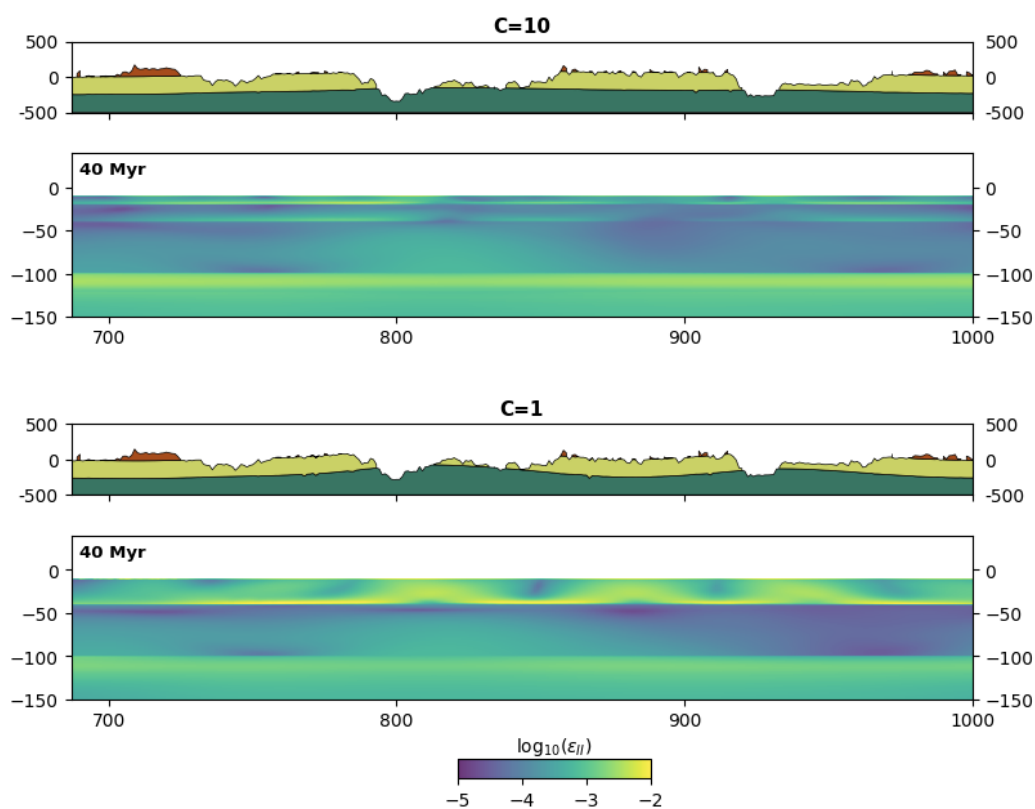


Figure 4.2: Patterns of strain accumulated over a simulation period of 40 Myr for the reference scenarios, as well as topographic curves and stratal geometries resulting from the respective simulations. Horizontal extent shown is limited to the region of the constraining profile (687 to 1000 km).

lower crust is subducted, characterized by low-relief, longer-wavelength features and very low curvature of the strata. Inversely, topographic features in the second simulation present shorter wavelength, more accentuated relief and visible stratal curvature.

Divergences between the deformational styles and topographic forms of the reference models can be explained by considering that smaller values of the compositional factor  $C$  for the lower crust imply lower viscosity values. As a consequence, lower crustal rocks become more easily mobilized under applied forces, accommodating a larger portion of the stresses imposed on the lithosphere by the removal of the material, and preventing these stresses to be efficiently transmitted to deeper lithospheric levels by means of the ductile flow of rocks within this layer (Burov and Diament, 1995).

## 4.2 *Off-profile denudation*

As mentioned earlier, a second set of simulations takes into account additional flexural loads due to removal of material from nearby off-profile regions by introducing artificial compensation zones within the sediment layer, the lateral extents of which are chosen to be approximately equal to those of the adjacent significantly denudated areas. One might expect the total uplift of the profile to be amplified, particularly in the zones of compensation. This, in turn, would cause other parts of the profile to subside due to lateral flow of subsurface material as a way to compensate for the increased magnitude of the applied flexural load.

Indeed, when the subsurface distribution of strain rate magnitudes is compared between scenarios changing only in the presence of these compensation zones (Figure 4.3), the similarity between the strain rate patterns in both simulations at a given instant becomes striking. High magnitudes are widespread, occurring throughout the domain in both models, although, it may be noted, these magnitudes are slightly increased in the simulation including the compensation zones. In spite of this marked difference in strain rates, which is sustained over the simulation period, the shape of the region presenting the highest values remain alike in the simulations under consideration, in terms of both width and depth.

The observed resemblance between the strain rate figures suggests that the main effect of introducing these zones is the “magnification” of this quantity and, hence, of the resulting surface uplift (Figure 4.4), the maximum amplitude of which is over twice as large in the scenarios accounting for off-profile removal with respect to the reference scenarios. Resemblant as they may be geometrically, the slight differences in the strain rate distributions for the scenarios with zones of compensation relative to those without them manifest superficially as smaller, noticeable features in the uplift pattern that are mostly absent in the reference simulations, but which are, nonetheless, relevant when comparing the results to the constraining profile. The shape of these features is, of course, controlled by the position and lateral extent assumed for each compensation zone. One example is the shift in the location of the maximum uplift, caused by the placement of the Vaza-Barris and Itapicuru compensation zones to the right (with reference to the profile view) of the previous maximum. Another interesting aspect is the “skewness” of the uplift associated with



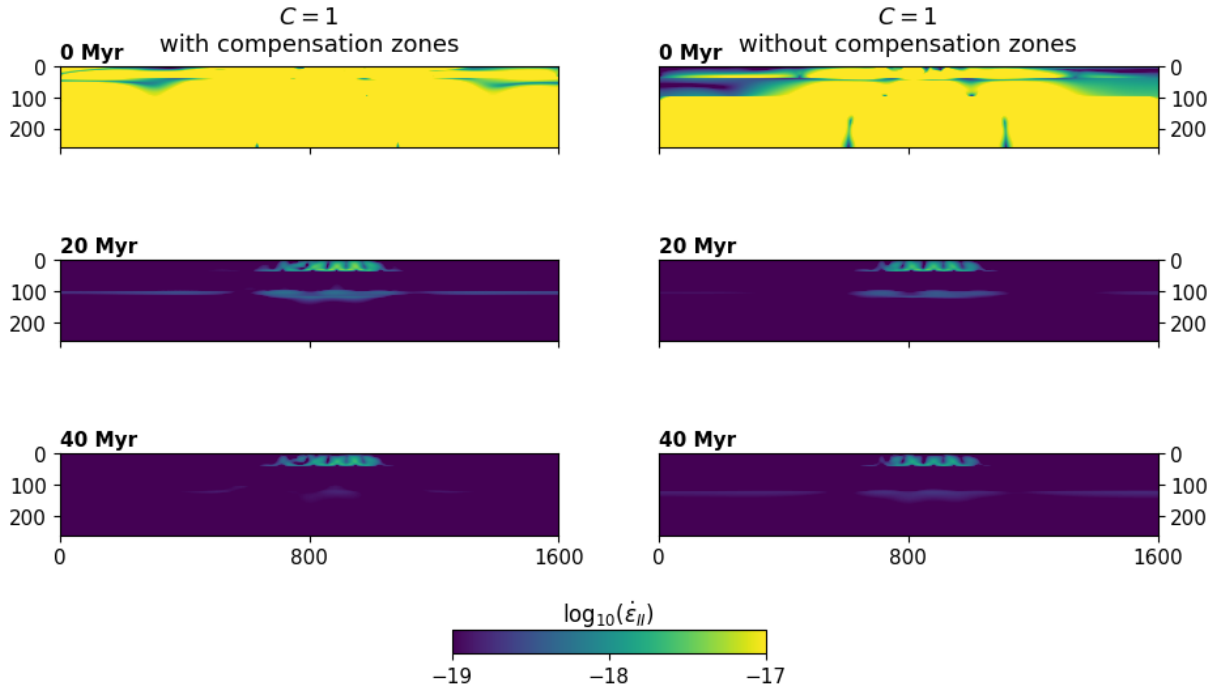


Figure 4.3: Evolution of the second invariant of the strain rate tensor for two scenarios with (left column) and without (right column) compensation zones. Both simulations feature  $C = 1$  for the lower crust.

the Vaza-Barris river valley: it is mostly absent in the reference scenarios, but becomes clearly visible when off-profile denudation is included, particularly for the simulation with  $C = 1$ . This asymmetry is aided by the presence of the Baixa do Chico Compensation Zone, which promotes additional uplift on the left side of the profile. Furthermore, regions of accentuated subsidence (negative uplift) are noted in the resulting uplift profile with lower degree of coupling, since the increased loads are accommodated by lower crustal flow.

A comparison of the topographic profiles resulting from different simulations with the geological profile from Freitas et al. (2017) (Figure 4.5e) allows us to make some observations regarding the adequacy of the models in question. The first and most immediately perceptible arises when one compares the curvature of the strata resulting from each model: it is clear that the real curvature of the Aptian layers is best reproduced in the model with compensation zones and  $C = 1$  for the lower crust (Figure 4.5d). A second important point to be marked is that the erosive envelope (corresponding to the uplift curve) in Figure 4.5d is evidently a much closer fit to the actual envelope from Freitas et al. (2017) (blue dashed curve in the figure) compared to the reference models (Figure 4.5b, c), with over 75% of the maximum uplift being successfully simulated in the presented scenario with off-profile denudation. One other noteworthy feature is the plateau located at the position

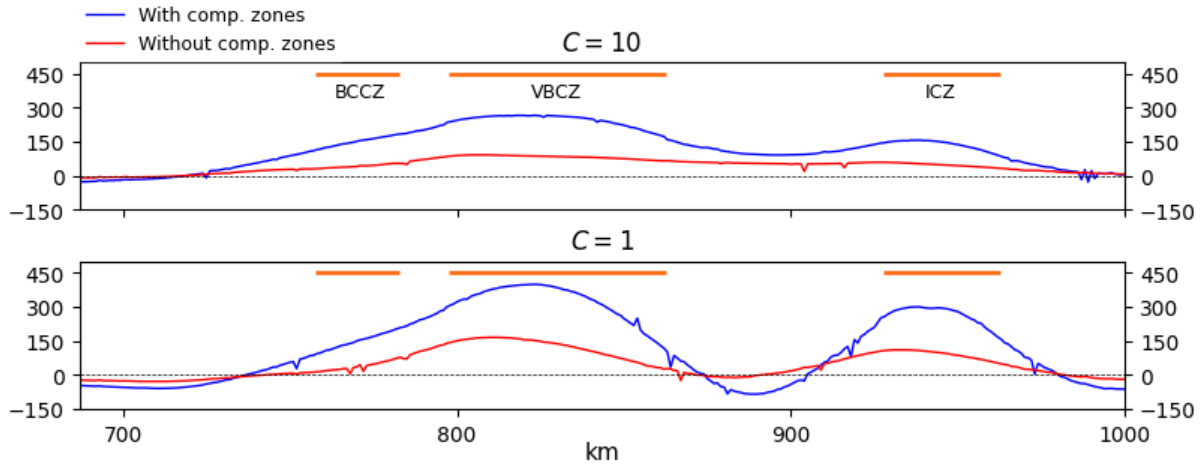


Figure 4.4: Modelled uplift for scenarios with lower crustal  $C$  of 10 (upper panel) and 1 (lower panel), with (blue curves) and without (red curves) off-profile denudation. Orange horizontal lines mark the location and extent of compensation zones. BCCZ = Baixa do Chico Compensation Zone, VBCZ = Vaza-Barris Compensation Zone, ICZ = Itapicuru Compensation Zone.

$\sim 700$  km (referred to in Freitas et al. (2017) as Tonã Plateau): this topographic feature represents a positive flexural load with respect to areas of rock removal, thus constituting a region subject to subsidence. This is made visible by considering that the base of this plateau coincides with the real envelope in Figure 4.5e, and looking closely at the difference between the modelled and real envelopes in this region for each scenario. The subsidence of the plateau is better adjusted in Figure 4.5d, which serves as further indication of the importance of the three-dimensional shape of the denudation in the basin system.

### 4.3 Degree of lithospheric coupling

As shown in the previous section, the distribution of surface loads acting on the model lithosphere is of primary importance in shaping the features that compose the resulting landscape. However, it is clear from earlier mentions that the response of the lithosphere to applied forces (tectonic or otherwise) is also strongly controlled by its rheological setting, particularly the degree of lithospheric coupling expressed by the value of the viscosity scaling factor  $C$  for the lower crust. This occurs because the mechanical behavior of lower crustal rocks determines the depth to which stresses associated with loads applied on the surface are balanced.

In light of this, several simulations were run differing strictly in the scaling factor  $C$  assumed for the lower crust, with the purpose of investigating which value of this parameter

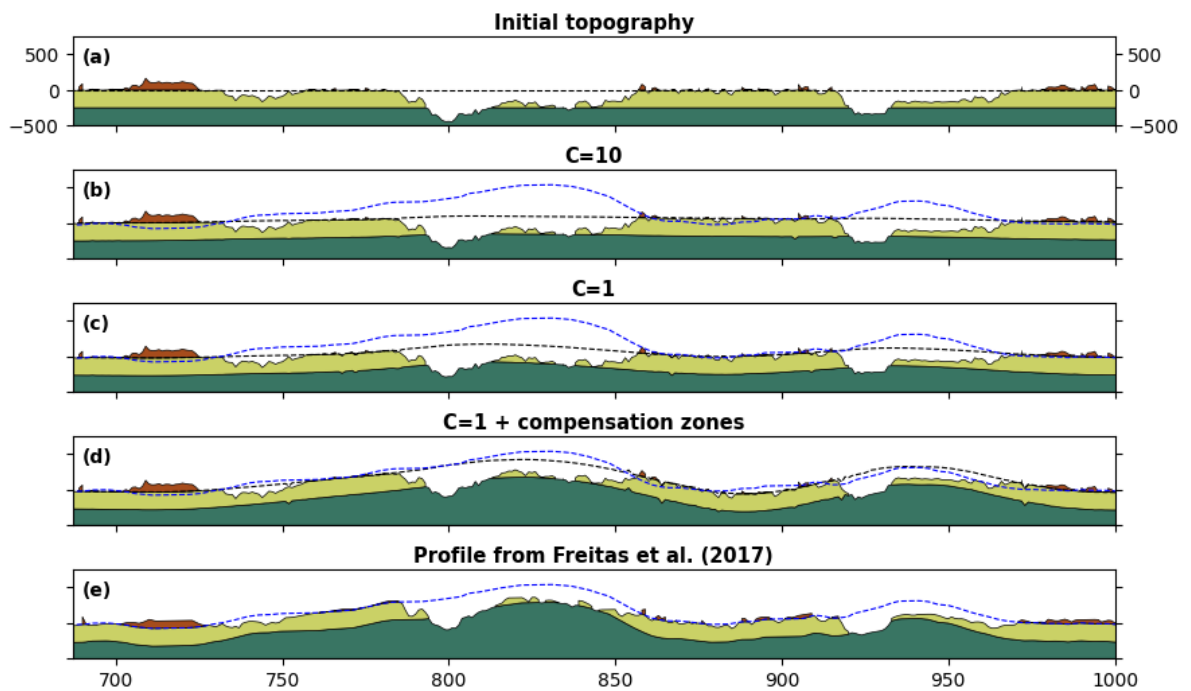


Figure 4.5: (a) Initial model topography and envelope (black dashed curve); (b-c) topographic and envelope curves resulting from the reference simulations; (d) final curves for a scenario accounting for off-profile denudation with  $C = 1$  for the lower crust; (e) Geologic profile and erosive envelope from Freitas et al. (2017), reduced of the regional component. The observed erosive envelope (blue dashed curve) is plotted in panels b-d for comparison.

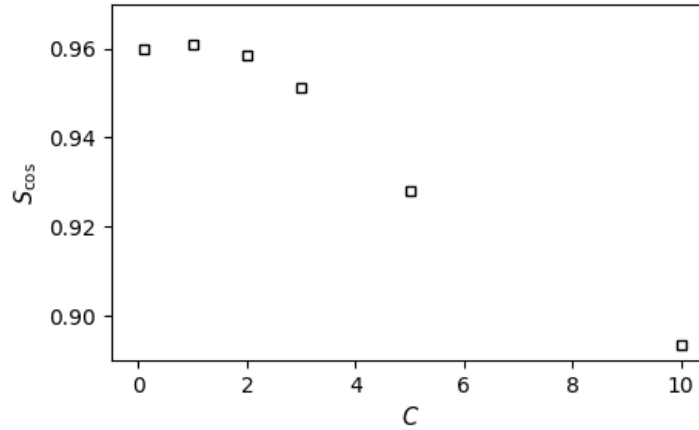


Figure 4.6: Cosine similarity as a function of the lower crustal viscosity scaling factor  $C$ .

provides an adequate fit for the actual topography. This evaluation makes use of the concept of cosine similarity between two vectors  $\mathbf{x}$  and  $\mathbf{y}$ , defined as:

$$S_{\cos}(\mathbf{x}, \mathbf{y}) = \frac{\mathbf{x} \cdot \mathbf{y}}{|\mathbf{x}||\mathbf{y}|}. \quad (4.1)$$

Equation 4.1 expresses the cosine of the angle between two vectors with any number of components, thus taking only values in the range -1 to 1. It is to be interpreted in the following manner: values closer to 1 imply that the input vectors have more similar directions and, thus, are more closely aligned. When the input vectors correspond to the observed and modelled uplift curves, the cosine similarity provides a measure of the “likeness” between these curves, and can be used for determining which model best fits the constraints, i.e., the one that maximizes the similarity. It must be mentioned that the cosine similarity is usually employed in circumstances where the magnitude of the input vectors (here represented by the uplift amplitude) is less important than their respective directions (here controlled by the lateral distribution of the uplift).

The adopted criterion allows us to note some aspects, as illustrated in Figure 4.6. Firstly, high values of  $C$  are associated with a low similarity, due to lower amplitudes of the simulated maximum uplift, as well as longer wavelengths in comparison to the real curve. A second noteworthy point is that, for  $C > 2$ , the similarity starts to decrease dramatically, while for  $C \leq 2$  the similarity shows little variation, being maximized for  $C = 1$ . This is mostly due to the fact that wavelength values for the uplift in scenarios with the lowest degrees of coupling do not differ significantly among them.

Regarding the maximum uplift in each simulation, we have noticed greater values in

scenarios where coupling between the upper crust and the lithospheric mantle is weaker, with up to 75% of the maximum observed uplift being reproduced in these models. Uplift in these scenarios is also less distributed laterally, being largely concentrated near the incised valleys, which reflects the accommodation of isostatically imposed stresses as viscous flow of material in lower crustal depths.

At this point it is worth stressing that, as a consequence of the instant removal of surface material at the beginning of the simulations, strain rate magnitudes throughout the model domain during the first few million years are expressively higher than they would be in the case of a temporally distributed removal (i.e., incorporating finite rates of denudation). The ductile viscosity (and, hence, the effective viscosity) of the lower crust presents significant nonlinear dependence on strain rate. In particular, as shown in Burov and Diament (1995), the yield strength of the lithosphere is significantly enhanced by higher strain rates, implying that, in the simulations here presented, the value obtained for lower crustal  $C$  may be somewhat lower than what would be estimated in scenarios including surface processes at finite rates. This has no bearing on the result that the presence of observed landforms in the studied region requires a low degree of lithospheric coupling, and, thus, I speculate that the addition of time-distributed erosion into the simulations would not bring a significant raise in the estimated value of  $C$  for the lower crust.

#### 4.4 Discussion

It is fruitful to discuss the deformation of the Aptian units of the RTJ from a flexural viewpoint, thus furnishing ground for comparison with the results of the thermomechanical simulations. This is done by approximating the behavior of the lithosphere by that of a thin elastic plate overlying an inviscid substratum, producing an elastic-type lithospheric rheology (Watts, 2001; Turcotte and Schubert, 2014). This abstraction has, of course, its own set of limitations, but provides valuable insight into the mechanical behavior of the lithosphere from a relatively simple mathematical framework.

As a starting point for the flexural analysis, let us consider the equation describing the deflection of an elastic plate subjected to a periodic load (Watts, 2001):

$$D \frac{d^4 w}{dx^4} + (\rho_m - \rho_i) g w = (\rho_c - \rho_i) g h \cdot \cos(2\pi x / \lambda_w) \quad (4.2)$$

where  $w$  is the deflection of the plate at position  $x$ ,  $D$  is the flexural rigidity of the plate,

$\rho_m$ ,  $\rho_i$  and  $\rho_c$  are the respective densities of the mantle, the material infilling the depression, and the load,  $h$  is the peak-to-trough amplitude of the applied surface load, and  $\lambda_w$  is its wavelength. This formulation presumes a constant rigidity for the whole plate, which is a reasonable assumption in this case, given the axial extent of the RTJ. The flexural rigidity may also be expressed as

$$D = \frac{ET_e^3}{12(1 - \nu^2)},$$

$E$  being the modulus of elasticity,  $\nu$  Poisson's ratio, and  $T_e$  the effective elastic thickness.

Upon substituting in Equation 4.2 a function of the form

$$w(x) = A_1 \cdot \cos(2\pi x/\lambda_w) + A_2 \cdot \sin(2\pi x/\lambda_w),$$

$A_1$  and  $A_2$  as constants to be determined, one finds the particular solution

$$w(x) = \left( \frac{\rho_c - \rho_i}{\rho_m - \rho_i} \right) h \cos(2\pi x/\lambda_w) \phi_e(\lambda_w) \quad (4.3)$$

$$\phi_e(\lambda_w) = \left[ 1 + \frac{D(2\pi/\lambda_w)^4}{(\rho_m - \rho_i)g} \right]^{-1}.$$

The factor  $\phi_e$  appearing in Equation 4.3 is termed *flexural response function*. It controls the deflection of the plate (output) to a given load (input), acting so as to “modify” the local isostatic compensation to produce the regional flexure of the plate.

From Equation 4.3 one may calculate the curvature of the plate as the absolute value of the second derivative of  $w(x)$ :

$$\left| \frac{d^2w}{dx^2} \right| = \left( \frac{\rho_c - \rho_i}{\rho_m - \rho_i} \right) \frac{4\pi^2 h}{\lambda_w^2} \cos(2\pi x/\lambda_w) \phi_e(\lambda_w) \quad (4.4)$$

which attains a maximum value of

$$K \equiv \max \left| \frac{d^2w}{dx^2} \right| = \left( \frac{\rho_c - \rho_i}{\rho_m - \rho_i} \right) \frac{4\pi^2 h}{\lambda_w^2} \phi_e(\lambda_w). \quad (4.5)$$

The approximate wavelengths for the loads related to removal along the Vaza-Barris and Itapicuru valleys are  $\sim 80$  and  $\sim 30$  km, respectively. The maximum curvature values associated with these uplifted regions are in the range  $5 - 10 \times 10^{-7} \text{ m}^{-1}$  (Figure 4.7). Taking  $\rho_c = 2700 \text{ kg.m}^{-3}$ ,  $\rho_m = 3300 \text{ kg.m}^{-3}$ ,  $\rho_i = 0 \text{ kg.m}^{-3}$  (since the flexurally subsiding areas are filled with air), a load with peak-to-trough amplitude of  $2h = 400$  m (consistent with the post-rift denudation in the RTJ), the maximum curvature values calculated using Equation 4.5 for the wavelength interval  $\lambda_w = 30 - 80$  km and  $T_e = 3$  km and  $T_e = 5$  km

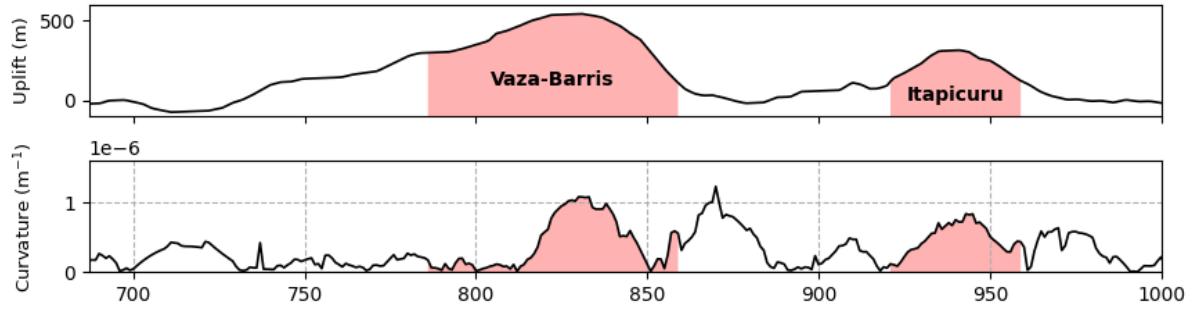


Figure 4.7: Uplift curve along the profile from Freitas et al. (2017) (upper panel), and absolute value of the local curvature of the uplift (lower panel). Curvature values are calculated as the absolute value of the second derivative of the uplift approximated by means of a second-order finite difference approximation. The curve in the lower panel was smoothed using a Savitzky-Golay filter with a window size of 101 points and polynomial degree of 5. Red patches indicate the approximate wavelength of the uplift “pulses” associated with the Vaza-Barris and Itapicuru incisions.

fall between  $5 - 8 \times 10^{-7} \text{m}^{-1}$  and  $1 - 5 \times 10^{-7}$ , respectively (Figure 4.8). For the same wavelength values, if  $T_e = 12 \text{ km}$  and  $T_e = 25 \text{ km}$ , the maximum curvatures are  $< 5 \times 10^{-8} \text{ m}^{-1}$  and  $< 1 \times 10^{-8} \text{ m}^{-1}$ . Moreover, if  $R$  represents the radius of curvature of a given surface, one can make the approximation  $K \approx 1/R$ . Considering Earth’s mean radius to be  $R_{Earth} = 6371 \text{ km}$ , its mean curvature is roughly  $K_{Earth} = 1.57 \times 10^{-7} \text{ m}^{-1}$ . What is implied by this is that, for sufficiently high values of the effective elastic thickness (in this case, 12 km is high enough), the curvature of landforms produced by flexural response of the lithosphere to denudation will be smaller than Earth’s mean curvature, and these topographic features will appear only as relatively subtle variations in the surface, their identification being further precluded by the action of erosive processes. This points at low  $T_e$  values ( $\leq 5 \text{ km}$ ) as a necessary condition for the occurrence of landforms with noticeable curvature and wavelengths as short as a few tens of km. Furthermore, the values estimated for the curvature of the uplift over the Vaza-Barris and Itapicuru valleys are best recreated when assuming low  $T_e$ .

Effective elastic thickness values estimated for continental regions range from only a few km to over 100 km, with a seemingly bi-modal distribution (Watts, 1992) characterized by peaks occurring at 10 – 20 km and 80 – 90 km. This distribution reflects the relation of  $T_e$  with the tectonic setting of the lithospheric plate: high values are usually associated with cratonic regions, whereas lower values would be mostly coincident with areas affected by rifting and other tectonic processes. Values  $\lesssim 5 \text{ km}$  correspond to less than 10% of the cases, suggesting that the preservation of relatively high-relief, short-wavelength

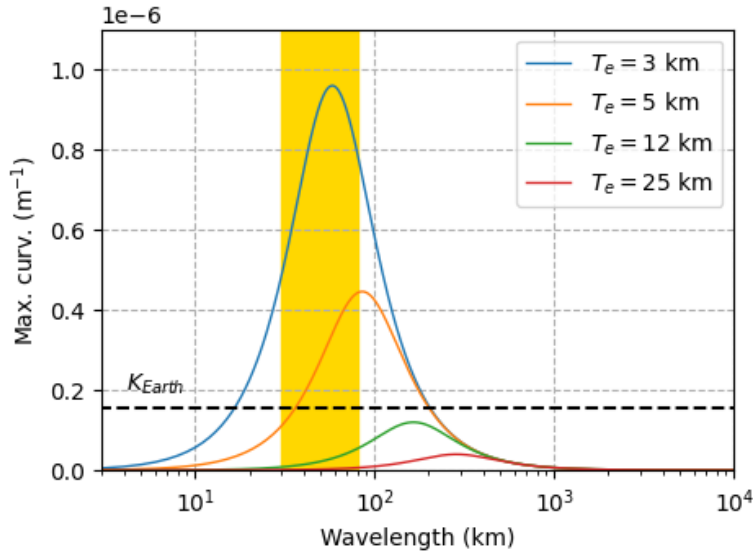


Figure 4.8: Maximum curvature of a plate subject to periodic loading as a function of load wavelength for different  $T_e$  values (3, 5, 12, and 25 km). Black dashed line indicates Earth's mean curvature, and the wavelength interval compatible with the uplift over the Vaza-Barris and Itapicuru valleys is indicated by the yellow patch.

flexural topographic features induced by material removal along *local* fluvial incisions may be exceptional and only identifiable in areas where the flexural rigidity is low.

A low flexural rigidity is in alignment with the results obtained from the thermomechanical simulations presented in previous sections. This is because these results indicate that the lithosphere beneath the RTJ must be weakly coupled in order to accurately reproduce the observed topography, implying that much of the compensation occurs through ductile deformation of lower crustal rocks. Therefore, the equivalent elastic plate representing the lithosphere must be considerably thin.

Decoupling of the lithosphere might be caused, for instance, by a combination of significant alterations in the lithospheric temperature structure at some point of its evolution, and lithological (compositional) aspects. Evidence for thermal perturbation in the form of magmatic underplating, as proposed by Magnavita et al. (1994), is provided by Alvarez and Holz (2022) and Döring et al. (2022). A description for the evolution of the temperature field in an infinite region subsequent to the solidification of a magmatic intrusion (in this case, the underplate sill) is provided by the analytical solution to the one-dimensional, time-dependent heat conduction equation (Turcotte and Schubert, 2014):

$$T(z, t) = T_0 + \frac{Q}{2\rho c\sqrt{\kappa t}} e^{-z^2/4\kappa t} \quad (4.6)$$



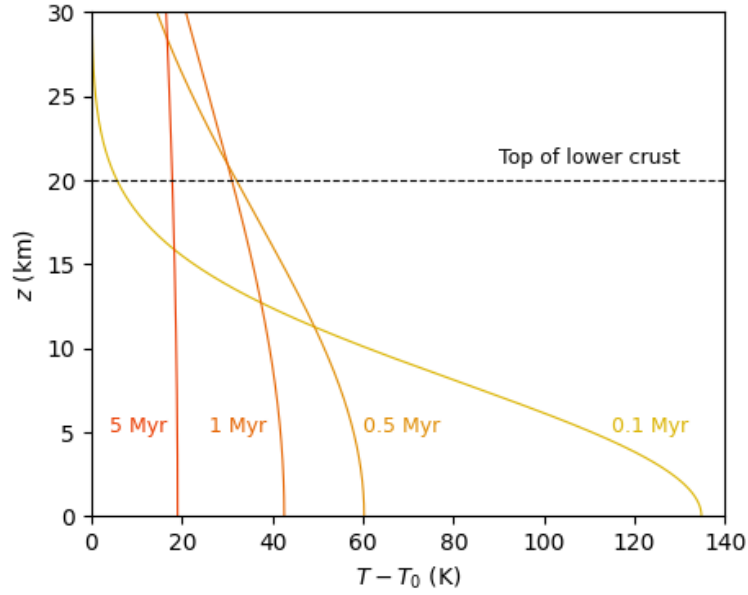


Figure 4.9: Distribution of the thermal perturbation ( $T - T_0$ ) with depth calculated using Equation 4.6 for  $t = 0, 1, 0.5, 1$  and  $5$  Myr. Horizontal dashed line indicates the top of the lower crust (thickness of  $20$  km) assuming the underplating occurs immediately beneath its base.

where  $z$  is the vertical distance between the planar heat source and the point under consideration,  $Q$  is the heat content of the magmatic body per unit of surface area

$$Q = \rho[c(T_u - T_0) + L]h_u,$$

$T_u$  is the melting temperature of the magma composing the underplating,  $T_0$  is the initial temperature of the country rock,  $L$  is the latent heat of fusion,  $h_u$  is the thickness of the underplating, and  $\rho$  and  $c$  are, respectively, the density and specific heat for the magma. Taking  $h_u = 3.5$  km (Alvarez and Holz, 2022),  $T_u - T_0 = 500$  K,  $\rho = 2800$  kg m<sup>-3</sup>,  $c = 1.2$  kJ kg<sup>-1</sup> K<sup>-1</sup>,  $L = 320$  kJ kg<sup>-1</sup>, and  $\kappa = 1 \times 10^{-6}$  m<sup>2</sup> s<sup>-1</sup>, the temperature difference  $T - T_0$  may be calculated as a function of the distance from the heat source for different time instants.

As shown in Figure 4.9, after only  $500$  kyr the magnitude of the thermal perturbation becomes smaller than  $100$  K, pointing that the influence of the underplating on the lower crustal thermal configuration might be short-lived and decay quite rapidly. This suggests that thermal effects associated with a subcrustal magmatic intrusion cannot be held entirely responsible for the low degree of lithospheric coupling supported by the numerical results, although this transient component may have contributed to the temporary weakening of the lower crust. Nevertheless, if the underplating occurred in the post-rift phase of

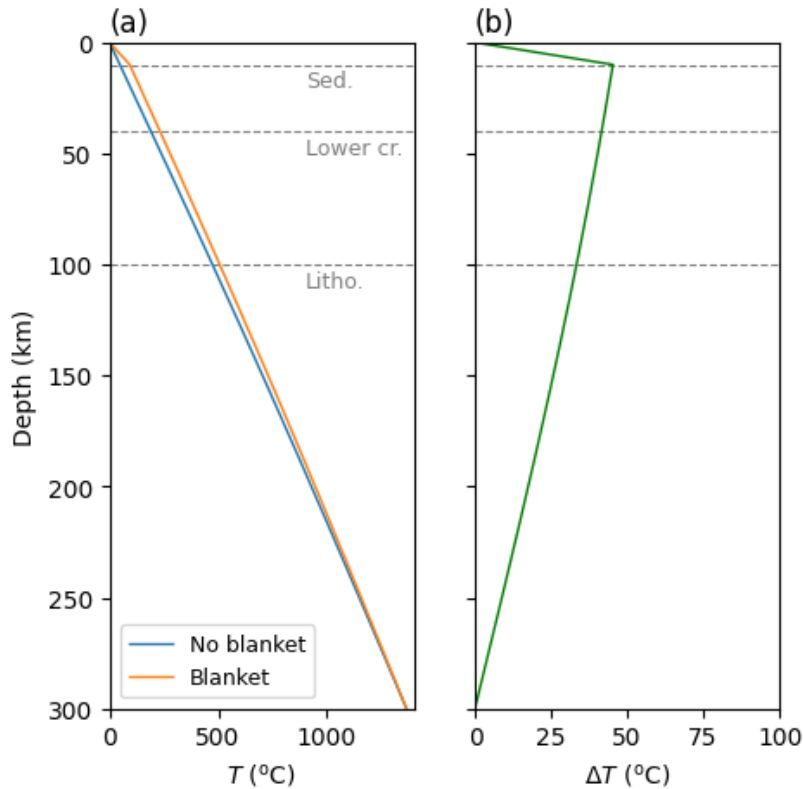


Figure 4.10: (a) Steady-state temperature profiles with (orange) and without (blue) sedimentary thermal blanketing, calculated by a simple numerical code using the finite difference approximation to the one-dimensional heat conduction equation, assuming adiabatic temperature increase in the asthenosphere; (b) temperature difference  $\Delta T$  between the profiles in (a).

the basin system, as held in Magnavita et al. (1994), then the magmatic intrusion beneath the crust may have promoted regional uplift. The relief created by large-scale uplift would, in turn, imply higher denudation rates shortly after the magmatic event, with the lower crust still thermally weakened, hence causing the short-wavelength flexural uplift observed at the valley flanks.

The presence of a thick sedimentary package filling the basin, as in the case of the RTJ, may also contribute to weaken the lithosphere, as a consequence of its lower thermal conductivity with respect to the underlying layers. This happens because the heat is transferred less efficiently through the sedimentary layer, which permanently raises subsurface temperatures and, hence, decreases the viscosity of the lower crust. However, even for a thick (10 km) layer, the temperature increase in lower crustal levels, with respect to a circumstance where thermal blanketing is not accounted for, is of the order of 50°C (Figure 4.10). This means that the effect of the overlying sediments on the crustal geotherm, although significant, is also unable to explain, by itself, the low viscosity required for the

---

lower crust in order to produce the geomorphic features studied here.

Lastly, one mechanism which might offer an explanation for the lithospheric weakening implied by the numerical results is the event of metasomatism in the lower crust associated with the crustal thinning and subsequent underplating. As the underplating takes place, magmatic fluids might rise from the intruding body and into the overlying lower crust, possibly being transported along grain boundaries and/or permeable structures. At the same time, crustal minerals are chemically altered, and often hydrated, during reactions with the ascending hot fluid (Harlov and Austrheim, 2013). This may cause the viscosity of rocks to be reduced, wherefrom the low value of the lower crustal  $C$  found to fit the observations. It must be stressed that, although plausible, the referred mechanism is merely speculated in the present work, and no attempt has been made here to verify its occurrence.



## Conclusions

Numerical thermomechanical modelling was performed in order to study lithosphere-scale dynamics during the post-rift stage of the Recôncavo-Tucano-Jatobá basin system, using a geologic-erosive profile of the Aptian sedimentary units as the main constraint. The adopted approach consisted of running several simulations with different rheological configurations for the model lithosphere and varying surface loads, with the aim of explaining as closely as possible the presence of certain geomorphic features in the studied region, particularly the relief pattern of fluvial valley flanks. The adequacy of a given numerical scenario to observations was evaluated based on the cosine similarity between the simulated and observed uplift curves. A second factor used for verifying the fitness of each scenario is the likeness between the curvature of the strata, representing the curvature of a thin elastic plate, produced by the simulation and that recorded in the geologic profile.

It is found that, within the assumptions of the model, the observed landforms are more faithfully reproduced in scenarios for which the degree of lithospheric coupling is low and the deformational regime is characterized by strain localized mainly in crustal layers, with roughly 75% of the maximum uplift being accounted for in a model with the viscosity scaling factor  $C = 1$  for the lower crust. This lithospheric decoupling may be partly due to the occurrence of magmatic underplating in the region, as suggested by Magnavita et al. (1994) and supported by Alvarez and Holz (2022) and Döring et al. (2022), aided by the thermal effect of the thick sedimentary package in the basin system. What's more, based on the equivalent thin elastic plate approach, inspection of the maximum curvature attained by the plate for different values of the effective elastic thickness ( $T_e$ ) when subjected to a load representative of the sediment removal along the RTJ main river valleys points at a value of  $T_e \leq 5$  km, in good agreement with the value obtained by Magnavita et al.

(1994). It is also hypothesized that metasomatism within the lower crust may have had an important influence in the rheological behavior of the lithosphere beneath the RTJ.

An important conclusion is that the topographic expression of the flexural-isostatic adjustment of the lithosphere in response to denudation along individual fluvial incisions, as in the case of the landforms observed in the RTJ, is only noticeable in the landscape provided that the rigidity of the lithosphere is low, which might occur in the studied region due to a combination of thermal and compositional factors.

## Bibliography

- Alkmim F. F., Martins-Neto M. A., Proterozoic first-order sedimentary sequences of the São Francisco craton, eastern Brazil, *Marine and Petroleum Geology*, 2012, vol. 33, p. 127
- Almeida F. F. M., Hasui Y., Brito Neves B. B., Fuck R. A., Brazilian structural provinces: an introduction, *Earth-Science Reviews*, 1981, vol. 17, p. 1
- Almeida Filho R., Miranda F., Digital image processing and enhancement of gravity data as an aid to the definition of the structural framework of the north Tucano-Jatobá basins, Northeastern Brazil, *Boletim IG-USP. Série Científica*, 1997, vol. 28, p. 121
- Alvarez P., Holz M., The Tucano Basin (Cretaceous, Brazil)—a world-class example of an aborted rift system with anomalous depth, *Journal of South American Earth Sciences*, 2022, vol. 119, p. 103975
- Balay S., Abhyankar S., Adams M., Brown J., Brune P., Buschelman K., Dalcin L., Dener A., Eijkhout V., Gropp W., et al., 2019 Technical report PETSc users manual. Argonne National Laboratory
- Bishop P., Long-term landscape evolution: linking tectonics and surface processes, *Earth Surface Processes and Landforms: the Journal of the British Geomorphological Research Group*, 2007, vol. 32, p. 329
- Blaich O. A., Tsikalas F., Faleide J. I., Northeastern Brazilian margin: Regional tectonic evolution based on integrated analysis of seismic reflection and potential field data and modelling, *Tectonophysics*, 2008, vol. 458, p. 51

- Braun J., Pecube: A new finite-element code to solve the 3D heat transport equation including the effects of a time-varying, finite amplitude surface topography, *Computers & Geosciences*, 2003, vol. 29, p. 787
- Braun J., A review of numerical modeling studies of passive margin escarpments leading to a new analytical expression for the rate of escarpment migration velocity, *Gondwana Research*, 2018, vol. 53, p. 209
- Brooks A. N., Hughes T. J., Streamline upwind/Petrov-Galerkin formulations for convection dominated flows with particular emphasis on the incompressible Navier-Stokes equations, *Computer methods in applied mechanics and engineering*, 1982, vol. 32, p. 199
- Brune S., Rifts and rifted margins: A review of geodynamic processes and natural hazards, *Plate Boundaries and Natural Hazards*, 2016, pp 11–37
- Burov E., Poliakov A., Erosion and rheology controls on synrift and postrift evolution: Verifying old and new ideas using a fully coupled numerical model, *Journal of Geophysical Research: Solid Earth*, 2001, vol. 106, p. 16461
- Burov E. B., Diament M., The effective elastic thickness ( $T_e$ ) of continental lithosphere: What does it really mean?, *Journal of Geophysical Research: Solid Earth*, 1995, vol. 100, p. 3905
- Caixeta J. M., Bueno G. V., Magnavita L. P., Feijó F., Bacias do reconcavo, tucano e jatoba, *Boletim de Geociências da PETROBRAS*, 1994, vol. 8
- Caputo M. V., Santos R. O. B., Stratigraphy and ages of four Early Silurian through Late Devonian, Early and Middle Mississippian glaciation events in the Parnaíba Basin and adjacent areas, NE Brazil, *Earth-Science Reviews*, 2020, vol. 207, p. 103002
- Castro A. C. M. J., The northeastern Brazil and Gabon basins: a double rifting system associated with multiple crustal detachment surfaces, *Tectonics*, 1987, vol. 6, p. 727
- Chemale F. J., Roque N. C., Cupertino J. A., Analysis of the major structural features of the Southern and Central Tucano sub-basins, Bahia, *Geociências*, 1994, vol. 13, p. 405



- Costa I., Milhomem P. d. S., Bueno G. V., Silva H., Kosin M. D., Sub-bacia de Tucano Norte e Bacia de Jatobá, *Boletim de Geociências da PETROBRAS*, 2007a, vol. 15, p. 445
- Costa I., Milhomem P. d. S., Bueno G. V., Silva H., Kosin M. D., Sub-bacias de Tucano Sul e Central, *Boletim de Geociências da PETROBRAS*, 2007b, vol. 15, p. 433
- Cramer F., Schmeling H., Golabek G., Duretz T., Orendt R., Buitter S., May D., Kaus B., Gerya T., Tackley P., A comparison of numerical surface topography calculations in geodynamic modelling: an evaluation of the ‘sticky air’ method, *Geophysical Journal International*, 2012, vol. 189, p. 38
- Döring M., Julià J., Evain M., Joint inversion of receiver functions and surface wave dispersion in the Reconcavo-Tucano basin of NE Brazil: implications for basin formation, *Geophysical Journal International*, 2022, vol. 230, p. 317
- Figueiredo F. T., Almeida R. P., Freitas B. T., Marconato A., Carrera S. C., Turra B. B., Tectonic activation, source area stratigraphy and provenance changes in a rift basin: the Early Cretaceous Tucano Basin (NE-Brazil), *Basin Research*, 2016, vol. 28, p. 433
- Freitas B. T., Almeida R. P., Carrera S. C., Figueiredo F. T., Turra B. B., Varejao F. G., Assine M. L., Aptian sedimentation in the Recôncavo-Tucano-Jatobá Rift System and its tectonic and paleogeographic significance, *Journal of South American Earth Sciences*, 2017, vol. 80, p. 460
- Gawthorpe R., Hurst J. M., Transfer zones in extensional basins: their structural style and influence on drainage development and stratigraphy, *Journal of the Geological Society*, 1993, vol. 150, p. 1137
- Gerya T., *Introduction to numerical geodynamic modelling*. Cambridge University Press, 2010
- Gleason G. C., Tullis J., A flow law for dislocation creep of quartz aggregates determined with the molten salt cell, *Tectonophysics*, 1995, vol. 247, p. 1
- Gomes C. P. J., Fossen H., de Almeida R. P., Salmoni B., Subseismic deformation in the Vaza-Barris transfer zone in the Cretaceous Recôncavo-Tucano-Jatobá rift system, NE Brazil, *Journal of Structural Geology*, 2018, vol. 117, p. 81

- Gordon A., Destro N., Heilbron M., The Recôncavo-Tucano-Jatobá rift and associated Atlantic continental margin basins, São Francisco Craton, Eastern Brazil: Tectonic Genealogy of a Miniature Continent, 2017, pp 171–185
- Harlov D. E., Austrheim H., Metasomatism and the chemical transformation of rock: rock-mineral-fluid interaction in terrestrial and extraterrestrial environments. Springer, 2013
- Hughes T. J., The finite element method: linear static and dynamic finite element analysis. Courier Corporation, 2012
- Karato S.-i., Wu P., Rheology of the upper mantle: A synthesis, *Science*, 1993, vol. 260, p. 771
- Karner G. D., Egan S. S., Weissel J. K., Modeling the tectonic development of the Tucano and Sergipe-Alagoas rift basins, Brazil, *Tectonophysics*, 1992, vol. 215, p. 133
- Kaus B. J., Mühlhaus H., May D. A., A stabilization algorithm for geodynamic numerical simulations with a free surface, *Physics of the Earth and Planetary Interiors*, 2010, vol. 181, p. 12
- Kusznir N., Ziegler P., The mechanics of continental extension and sedimentary basin formation: a simple-shear/pure-shear flexural cantilever model, *Tectonophysics*, 1992, vol. 215, p. 117
- MacFerrin M. J., Amante C., Carignan K., Love M. R., Lim E., Arcos N. P., Stroker K. J., ETOPO 2022: NOAA's new seamless topography-and-bathymetry bare earth surface elevation dataset. In *AGU Fall Meeting Abstracts* , vol. 2022, 2022, p. NH22C
- McKenzie D., Some remarks on the development of sedimentary basins, *Earth and Planetary science letters*, 1978, vol. 40, p. 25
- Magnavita L., Cupertino J., A new approach to the geological configuration of the Lower Cretaceous Tucano and Jatobá basins, northeastern Brazil, *Revista brasileira de geociências*, 1988, vol. 18, p. 222
- Magnavita L. P., Geometry and kinematics of the Reconcavo-Tucano-Jatoba Rift, NE Brazil., University of Oxford, 1992, Ph.D. Thesis

- Magnavita L. P., Davison I., Kuszniir N. J., Rifting, erosion, and uplift history of the Recôncavo-Tucano-Jatobá Rift, northeast Brazil, *Tectonics*, 1994, vol. 13, p. 367
- Magnavita L. P., Szatmari P., Cupertino J. A., Destro N., Roberts D., The Recôncavo Basin, *Regional Geology and Tectonics: Phanerozoic Rift Systems and Sedimentary Basins*, 2012, pp 383–420
- Matos R. M. D., The northeast Brazilian rift system, *Tectonics*, 1992, vol. 11, p. 766
- Milani E. J., Davison I., Basement control and transfer tectonics in the Recôncavo-Tucano-Jatobá rift, Northeast Brazil, *Tectonophysics*, 1988, vol. 154, p. 41
- Miranda F. L. C., Cerqueira J. R., Amaral D. N., Abreu N. C., Góes V. C. M., Silva A. S., Dino R., Antonioli L., Queiroz A. F. d. S., dos Santos L. C. L., Garcia K. S., *Geoquímica Orgânica de Folhelhos da Formação Pojuca, Bacia do Recôncavo, Brasil*, *Anuário do Instituto de Geociências*, 2021, vol. 44
- Mohriak W. U., Bassetto M., Vieira I. S., Tectonic evolution of the rift basins in the northeastern Brazilian region, *Atlantic Rifts and Continental Margins*, *Geophys. Monograph*, 2000, vol. 115, p. 293
- Neumann V. H., Rocha D. E., Stratigraphy of the Post-Rift Sequences of the Jatobá Basin, Northeastern Brazil. In *STRATI 2013: First International Congress on Stratigraphy At the Cutting Edge of Stratigraphy* , 2014, p. 553
- Oliveira A. L. S., de Lira Santos L. C. M., Tedeschi M., Queiroga G., Viegas G., Cawood P. A., On the crustal framework of the central Alto Pajeú Terrane (Borborema Province, NE Brazil): Geophysical and structural data constrain late Neoproterozoic transpression in Western Gondwana, *Tectonophysics*, 2023, vol. 854, p. 229811
- Oliveira R. G., Medeiros W. E., Deep crustal framework of the Borborema Province, NE Brazil, derived from gravity and magnetic data, *Precambrian Research*, 2018, vol. 315, p. 45
- Palumbo F., Main I. G., Zito G., The thermal evolution of sedimentary basins and its effect on the maturation of hydrocarbons, *Geophysical Journal International*, 1999, vol. 139, p. 248

- Portela H. A., Antonioli L., Alvim R. M., Análise De Palinofácies Na Avaliação Do Potencial Gerador Da Formação Pojuca, Bacia Do Recôncavo, *Revista Brasileira de Paleontologia*, 2016, vol. 19, p. 271
- Rose I., Buffett B., Heister T., Stability and accuracy of free surface time integration in viscous flows, *Physics of the Earth and Planetary Interiors*, 2017, vol. 262, p. 90
- Sacek V., Post-rift influence of small-scale convection on the landscape evolution at divergent continental margins, *Earth and Planetary Science Letters*, 2017, vol. 459, p. 48
- Sacek V., Assunção J., Pesce A., Monteiro da Silva R., Mandyoc: A finite element code to simulate thermochemical convection in parallel, *Journal of Open Source Software*, 2022
- Salazar-Mora C. A., Sacek V., Effects of tectonic quiescence between orogeny and rifting, *Tectonics*, 2023, vol. 42, p. e2022TC007492
- Silva J. P. M., Sacek V., da Silva R. M., The influence of lithospheric rheology and surface processes on the preservation of escarpments at rifted margins, *Tectonophysics*, 2023, vol. 851, p. 229769
- Silva O. d., Caixeta J., Milhomem P. d. S., Kosin M. D., Bacia do recôncavo, *Boletim de Geociências da PETROBRAS*, 2007, vol. 15, p. 423
- Silva R. M., Sacek V., Influence of surface processes on postrift faulting during divergent margins evolution, *Tectonics*, 2022, vol. 41, p. e2021TC006808
- Tackley P. J., King S. D., Testing the tracer ratio method for modeling active compositional fields in mantle convection simulations, *Geochemistry, Geophysics, Geosystems*, 2003, vol. 4
- Theunissen T., Huisman R. S., Long-term coupling and feedback between tectonics and surface processes during non-volcanic rifted margin formation, *Journal of Geophysical Research: Solid Earth*, 2019, vol. 124, p. 12323
- Turcotte D. L., Schubert G., *Geodynamics*. Cambridge University Press, 2014
- Ussami N., Karner G. D., Bott M. H., Crustal detachment during South Atlantic rifting and formation of Tucano–Gabon basin system, *Nature*, 1986, vol. 322, p. 629

- 
- van Zelst I., Cramer F., Pusok A. E., Glerum A., Dannberg J., Thieulot C., 101 geodynamic modelling: How to design, carry out, and interpret numerical studies, *Solid Earth Discuss*, 2021, vol. 2021, p. 1
- Varejão F. G., Warren L. V., de Jesus Perinotto J. A., Neumann V. H., Freitas B. T., de Almeida R. P., Assine M. L., Upper Aptian mixed carbonate-siliciclastic sequences from Tucano Basin, Northeastern Brazil: Implications for paleogeographic reconstructions following Gondwana break-up, *Cretaceous Research*, 2016, vol. 67, p. 44
- Wangen M., The blanketing effect in sedimentary basins, *Basin Research*, 1994, vol. 7, p. 283
- Watts A., The effective elastic thickness of the lithosphere and the evolution of foreland basins, *Basin Research*, 1992, vol. 4, p. 169
- Watts A. B., *Isostasy and Flexure of the Lithosphere*. Cambridge University Press, 2001
- Wernicke B., Uniform-sense normal simple shear of the continental lithosphere, *Canadian Journal of earth sciences*, 1985, vol. 22, p. 108
- Wolf L., Huismans R. S., Rouby D., Gawthorpe R. L., Wolf S. G., Links between faulting, topography, and sediment production during continental rifting: Insights from coupled surface process, thermomechanical modeling, *Journal of Geophysical Research: Solid Earth*, 2022, vol. 127, p. e2021JB023490
- Zhong S., Yuen D. A., Moresi L. N., Schubert G., Numerical methods for mantle convection, *Treatise on geophysics*, 2007, vol. 7, p. 227